

Eirik Rådmannsøy Ulstein

Combined Waves and Tidal Current Flow over a Full Tidal Cycle

Master's thesis in Marine Technology
Supervisor: Lars Erik Holmedal
June 2019

NTNU
Norwegian University of Science and Technology
Faculty of Engineering
Department of Marine Technology

Eirik Rådmannsøy Ulstein

Combined Waves and Tidal Current Flow over a Full Tidal Cycle

Master's thesis in Marine Technology
Supervisor: Lars Erik Holmedal & Hong Wang
June 2019

Norwegian University of Science and Technology
Faculty of Engineering
Department of Marine Technology



Norwegian University of
Science and Technology

Preface

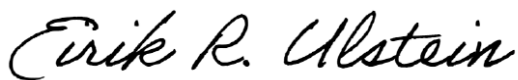
This master thesis is written during the spring of 2019 at the Department of Marine Technology at the Norwegian University of Science and Technology in Trondheim. It is the concluding work that marks the completion of my Master of Science degree in Marine Technology.

The process of writing this thesis has been very educational and challenging where I have improved my knowledge about hydrodynamics, physical oceanography and programming. I chose to write about oceanography and tidal currents because that is a topic that fascinates me, and I therefore wanted to learn more about it. I didn't have much programming experience before this work, making the process challenging, but educational as well.

I would like to express my gratitude towards my supervisor, Professor Lars Erik Holmedal for guidance throughout the semester and for providing me with the numerical model. I thank him for his patience related to my learning process within programming. I would also like to thank my co-supervisor Dr. Hong Wang for support related to the programming and for valuable discussions.

Finally, I would like to thank my fellow students, especially the ones at office A1.007, for a great last year at Tyholt.

Trondheim, June 11, 2019



Eirik Rådmannsøy Ulstein

Summary

The objective of present work is to be able to predict the effects of combined sinusoidal surface waves and tidal current flow over a full tidal cycle. A one dimensional two-equation numerical turbulence closure model has been used over intermediate water depth. The implementation of waves and current in present work is a one-way implementation, where the current initiates the combined boundary layer.

The model was, in a project thesis written during the fall of 2018, successfully validated for pure tidal flow with field data measurements presented by King and G. Davies A. (1985), and for the wave boundary layer with laboratory experiments by Jensen et al. (1989). The model was afterwards developed to be able to model the combined effects of waves and tidal current over a full tidal cycle. The most interesting, and most critical area in the water column is close to the sea-bed. Therefore, a finer mesh with more grid points has been added to the areas close to the boundary layer at the bottom. As the project thesis is not published, the most important results are given in Appendix A.

There exist various published material and work containing the combined waves and current boundary layer effects. However, the investigation of combined waves and tidal current over a full tidal cycle is a physical "multiscale" problem that has, to the author's knowledge, never been solved before. Field measurements for combined waves and tidal current over a full tidal cycle with sufficient quality have not been found prior to present work.

Particle trajectory investigation over a full tidal cycle shows that the combined waves and tidal current exhibit reduced velocities and thus reduced traveling distance compared to pure tidal current alone. The difference between the combined waves and tidal current ellipse and the ellipse for pure tidal current is much larger at 10 cm above the sea-bed in comparison with 23 cm above the sea-bed. The cause for this is assumed to be that the flow

at 10 cm above the sea-bed is closer to the wave-induced boundary layer on the sea-bed, which means that the apparent roughness have a greater influence on the flow closer to the sea-bed.

Close-up views of the combined waves and tidal current particle trajectories show that the ellipse exhibit a horizontal oscillatory pattern from side to side when the waves and tidal current interact with an angle between each other. This is assumed to be caused by a change in the generation of turbulent energy over a wave cycle.

The effect of increased bottom roughness z_0 showed to give a significant reduction in the traveling distance of the particles in the trajectory ellipses. This result shows that it is utterly important to know the sea-bed conditions in the area of evaluation.

Further work should include shear stress analysis of the sea-bed, mass transport by non-linear waves, introduce flux for the turbulent quantities and add a nonlinear interaction between the boundary layers for the waves and current.

Sammendrag

Målet for dette arbeidet er å kunne forutsi effektene fra kombinert sinusformede overflatebølger og tidevannsstrøm over en full tidevannssyklus. En en-dimensjonal turbulensmodell med to likninger har blitt brukt over middels vanddyb. Implementering av bølger og strøm er en enveis implementering, hvor tidevannet driver det kombinerte bunngrensesjiktet.

Modellen ble i en prosjektoppgave skrevet i løpet av høsten 2018 vellykket validert for ren tidevannsstrøm med feltdata presentert av King and G. Davies A. (1985), og for bølgegrensesjiktet med laboratorie eksperimenter av Jensen et al. (1989). Modellen ble senere utviklet for å kunne modellere de kombinerte effektene fra bølger og tidevannsstrøm over en full tidevannssyklus. Det mest interessante og mest kritiske området i vannsøylen er nært havbunnen. Derfor har et finere "mesh" med flere gitterpunkter blitt lagt til i områdene nært grensesjiktet på havbunnen. Fordi prosjektoppgaven ikke er publisert, er de viktigste resultatene lagt ved i Vedlegg A.

Det finnes ulike publiserte arbeider som omhandler det kombinerte grensesjiktet for bølger og tidevannsstrøm. Undersøkelse av kombinert bølge og tidevannsstrøm over en full tidevannssyklus er imidlertid et fysisk "multiscale" problem som, etter forfatterens viten, aldri før har blitt løst. Feltnålinger for kombinert bølger og tidevannsstrøm over en full tidevannssyklus med tilstrekkelig kvalitet har ikke blitt funnet for denne oppgaven.

Partikkelbaneundersøkelse over en full tidevannssyklus viser at den kombinerte bølge og tidevannsstrømmen viser reduserte hastigheter og dermed reduserte avstander sammenlignet med ren tidevannsstrøm alene. Forskjellen mellom ellipsen for kombinert bølge og tidevannsstrøm og ellipsen for ren tidevannsstrøm er mye større på 10 cm over havbunnen sammenlignet med for 23 cm over havbunnen. Årsaken til dette antas å være at strømmingen ved 10 cm over havbunnen er nærmere det bølgeinduserte grensesjiktet på havbunnen, noe som betyr at den bølgeinduserte ruheten (apparent roughness) har større

innflytelse på strømmen nærmere havbunnen.

Nærbilder av ellipsen for kombinerte bølger og tidevannsstrøm viser at ellipsen viser horisontale svinginger fra side til side når bølgene og tidevannsstrømmen virker med en vinkel mellom hverandre. Dette antas å være forårsaket av en endring i genereringen av turbulent energi over en bølgesyklus.

Effekten av økt bunnruhet z_0 viste seg å gi en betydelig reduksjon i avstanden partiklene beveget seg over. Dette resultatet viser at det er veldig viktig å kjenne forholdene til havbunnen ved det aktuelle området.

Videre arbeid bør omfatte skjærspennings-analyse av havbunnen, massetransport i ikke-lineære bølger, introdusere flux for turbulens og en ikke-lineær interaksjon mellom grensesjiktene for kombinert bølger og strøm.

Contents

1	Introduction	1
2	Tides	3
2.1	The Equilibrium Model of Tides	3
2.1.1	Combined Lunar and Solar Tides	7
2.2	The Coriolis Effect	9
2.3	The Dynamic model of Tides	10
2.4	Tidal Currents	12
3	Sea Environment	15
3.1	Wave Theory	15
3.1.1	Boundary conditions	16
3.2	Nonlinear Wave Effects	19
3.3	Wind Induced Currents	20
3.3.1	Ekman Layers	21
3.4	Interaction Between Waves and Currents	22
4	Boundary Layers	25
4.1	The boundary layer approximation	26
4.2	The low Rossby number approximation	28

5	Turbulence and Turbulence Modeling	29
5.1	The Reynolds Model	29
5.2	The Generalized Eddy Viscosity Concept	30
5.3	The Impact of Bottom Roughness	33
5.3.1	Universal Law of The Wall	34
6	Model Formulation	35
6.1	Governing Equations	35
6.2	Boundary Conditions	37
6.2.1	At the bottom	37
6.2.2	At the outer boundary	37
6.3	Forcing Function	39
6.4	Numerical method	40
7	Verification of the Model for Regular Waves Alone	41
8	Results and Discussion	45
8.1	Splined data from the model for pure tidal effects	46
8.2	Particle Trajectories	47
8.3	Effect of Bottom Roughness	51
9	Conclusion	55
10	Recommendations for further work	57
	Appendices	I
	Validation of the pure tidally driven flow model	III

List of Figures

2.1	The tidal bulges created by the moon. The figure is reproduced from J. Brown (1989)	4
2.2	Earth-moon system. a) The system with a fixed point P. b) The system seen from above. Figure from Grønningsæter (2015).	5
2.3	Tide producing forces: gravitational forces and centrifugal forces on the earth because of the moon. Figure from J. Brown (1989).	7
2.4	The earth-moon-sun system. Figure from J. Brown (1989).	8
2.5	Coriolis effect	10
2.6	The principle behind the dynamic model of tides. Figure from Pinet (2015).	11
2.7	Amphidromic systems in the North Sea. Figure from J. Brown (1989).	12
2.8	Fluid particles underneath a wave in deep (left) and finite water depth (right). Figure from Pettersen (2004).	13
2.9	Sketch of a current rose. The velocity vectors of a full tidal cycle will form a tidal ellipse. The vectors is plotted 20 times over a tidal cycle.	13
3.1	a) General structure of a 2D boundary value problem b) 2D water waves specified as a boundary value problem. Figure from Dean and Dalrymple (1991)	17

3.2	Orbital motion of fluid particles inducing mass transport. Figure from Myrhaug (2014).	19
3.3	Comparison of a stokian and linear wave profile. Figure from Myrhaug (2001)	20
3.4	The Ekman spiral. Figure from Pinet (2015).	21
3.5	Shear stress near the sea-bed for a combined waves and tidal current flow. Figure reproduced from (Soulsby, 1997)	23
4.1	Sketch of a laminar boundary layer. Figure from Schlichting and Gersten (2017).	26
6.1	Sketch showing the direction of the current and the waves	36
7.1	Comparison between modeled (lines) and measured (dotted lines) velocity profiles	42
7.2	Comparison between modeled (lines) and measured (dotted lines) profiles of turbulent kinetic energy	42
7.3	Comparison between modeled (lines) and measured (dotted lines) Reynolds shear stress profiles	43
7.4	Comparison between predicted (lines) and measured (dotted lines) friction velocity	43
8.1	Splined results (dotted lines) plotted against the input data (lines) of the horizontal and vertical velocities u and v , the turbulent kinetic energy k and the dissipation of turbulent kinetic energy ϵ	46
8.2	Trajectories for 10 and 23 cm above the sea-bed with $z_0 = 0.01$ cm and comparison with pure tidal current ellipses (dotted lines)	48
8.3	Close up of the combined waves and tidal current ellipse at 6 different positions. 10 cm above the sea-bed and with $z_0 = 0.01$ cm	50

8.4	The particle trajectory ellipses for combined waves and tidal current 10 cm above the sea-bed with two different values of roughness height. The numbers mark different intervals where mean velocity profiles have been extracted from	51
8.5	Mean velocity profiles for the intervals showed in Figure 8.4	52
8.6	Comparison between different values for roughness height z_0 . 10 cm above the sea-bed	53
A.1	Velocity time series. Filled lines is u from model, dotted line is v from model, stars are u from field data and circles are v from field data	V
A.2	Tidal velocity ellipses	VII
A.2	Continue	VIII

Abbreviations

DNS	=	Direct numerical simulations
NS	=	Navier Stokes
RANS	=	Reynolds Averaged Navier Stokes
LES	=	Large Eddy Simulations
BC	=	Boundary Conditions

Symbols

All symbols are defined in the below list, in addition to in the text, where they are defined the first time they occur.

ρ	Density of a fluid
$\vec{\omega}$	Angular velocity of the earth
Ω	Angular velocity of the earth-moon system
$\vec{a}_{P,abs}$	Absolute acceleration of a point P
$\vec{a}_{P,rel}$	Acceleration of a point P in a relative system
$\vec{v}_{P,rel}$	Velocity of a point P in a relative system
\vec{a}_E	Acceleration of the earth's center of mass
\vec{r}	Position vector of a point P in the earth-fixed relative coordinate system
\vec{r}_E	Vector from the earth center of mass to the earth-moon center of mass
\vec{a}_T	Acceleration of the axis T around the sun
m	Mass of water bulge
M	Mass of the moon
G	Gravitational constant
\vec{S}_0	The centrifugal force
\vec{G}	Gravitational force from the moon on a point P on earth
F	Force
τ_{turb}	Turbulent shear stress
u, v, w	Velocities in x, y and z directions
u_i	Velocities in x, y and z directions (i=1,2,3)
u_i', v_i'	Fluctuating velocity components
$\overline{u_i' u_j'}$	Reynolds stresses
μ	Dynamic viscosity
ν	Kinematic viscosity
f_u, f_v	Effect from Coriolis acceleration

ν_T	Eddy viscosity
δ	Boundary layer height
L	Length scale
U_0	Free stream velocity
f	Coriolis parameter
f_0	Coriolis parameter at a given latitude
$\delta_{i,j}$	Kronecker delta function
k	Turbulent kinetic energy
l_m	Mixing length
V_m	Velocity scale of the largest turbulent eddies
ϵ	Viscous dissipation rate of turbulent kinetic energy
L	Turbulent length
z_0	Roughness height
k_s	Nikuradse roughness
R_r	Reynolds roughness number
U_*	Turbulent velocity at sea bed
κ	Von Karman constant
τ_0	Sea-bed shear stress
λ	Wave length
ζ_A	Wave amplitude
$c_1, c_{\epsilon 1}, c_{\epsilon 2}, \sigma_k, \sigma_\epsilon$	Model constants
C_D, C_μ, C_1	Empirical constants
ζ	Wave elevation
ϕ	Velocity potential
W	Free stream velocity amplitude
W_0	Free stream velocity amplitude variation
U_c, V_c	Mean current velocity in x and y directions

Introduction

The gravitational forces from the moon and the sun create tides in the oceans. As the ocean surface rise and falls, enormous amounts of water will migrate over large distances, which gives rise to tidal currents. These currents can be quite powerful, especially over shallow grounds and canals. Tidal currents are important regarding transport of masses in the oceans, such as nutrition's, bottom materials, pollution and waste. They may also be of interest in the design of offshore structures.

Water particles in a current can be influenced by the presence of surface waves. The surface wave boundary layer will impact the current behavior, especially in coastal areas where particles induced by the boundary layer created by surface waves will impact the entire water column from the surface to the sea-bed. In Shallow water conditions, the flow can also be influenced by the bottom friction all the way to the surface. Bottom topography may also impose irregularities to the flow.

There exist many different simulation models to study the tidal flows and the wave boundary layer. Direct numerical simulations (DNS) and Large eddy simulations (LES) are two simulation methods that have been widely used to model the Navier Stokes (NS) equations in turbulent flows. However, these simulations require enormous amounts of computational power, and it is also challenging to include the effects from high Reynolds numbers and a rough bottom when using DNS or LES (Holmedal and Myrhaug, 2013). It is often therefore advantageous to use simplified models in the prediction of tidal flows. Several models have been used on the combined surface wave and tidal flow boundary layer.

Holmedal, Myrhaug, and Rue (2003) investigated the sea-bed boundary layer under random waves and current, using a one-dimensional turbulence model where the gridpoints are located in a line from the sea-bed to the surface. The model used by Holmedal and Myrhaug (2013) and Holmedal, Myrhaug, and Rue (2003) is the same model in use in present work.

The thesis is structured as follows. Chapter 2 - 5 include relevant background theory where some of the theory was written during a project thesis in the fall of 2018, with modifications in present work. Chapter 2 gives an introduction to the tide generating forces, and how tidal currents develop in the oceans. Chapter 3 gives an understanding of the sea environment, and how effects of waves and wind will influence the tidal currents. Chapter 4 gives an introduction to boundary layer theory and how scaling laws can be used to simplify the Navier Stokes equations. Turbulence theory and modeling are presented in Chapter 5. Tidal flows are typical turbulent, and knowledge about turbulence is therefore essential when it comes to the modeling of tidal flows. The turbulent model is presented in Chapter 6, with corresponding information about boundary conditions and forcing functions. In Chapter 7, the results from the sinusoidal wave boundary layer is presented. These results have been reproduced to verify the model for sinusoidal waves alone. Results from the combined sinusoidal waves and tidal flow model are presented and discussed in Chapter 8. The conclusion is presented in Chapter 9 and recommendations for further work is given in Chapter 10. The verification results of the model used in pure tidal flow are presented in Appendix A.

Tides

It is well known that all objects with a mass are drawn together by a gravitational pull. The earth, moon and sun pull on each other as a function of mass and distance between each other. Even though the sun is 10^7 times more massive than the moon, it has a much lower gravitational pull on the earth because of the long distance between them. The gravitational pull from the moon (lunar gravitational force) is the main force working on the tides together with the much smaller gravitational pull from the sun (solar gravitational force) (J. Brown, 1989). Because the moon is most important with regard to the tide varying forces, the focus will be on the lunar gravitational force regarding to the basic forces creating the tides. The moon rotates around the earth-moon combined center of mass with a period of 27.3 days in the same direction as the earth's rotation around its own axis. Combined with the earth rotation of 24 hours, a lunar day will have a period of 24 hours and 50 minutes and is the reason why the high and low tides appear at different times from day to day (Garrison, 2007).

2.1 The Equilibrium Model of Tides

The equilibrium model of tides is a simplified but useful model to describe the tidal variations on an ideal earth. The equilibrium model of tides is based on three main assumptions:

1. The earth is completely covered with seawater to an infinite depth, such that the

effects of coastlines and the effect from the seafloor is neglected.

2. The waves associated with the tides are assumed to be progressive waves.
3. The water is assumed to be in equilibrium with the tide generating forces (gravitational attractions and centrifugal effects) at all times.

It is also common to neglect the gravitational pull from the sun in the equilibrium model in order to simplify the calculations.

The lunar gravitational force is pulling the water on earth to the side where the moon is positioned at the present moment. This causes a tidal bulge of water resulting in a high tide at that side of the earth. At the same time, there exists a second tidal bulge on the opposite side of the earth. This tidal bulge is caused by a centrifugal effect created because the earth and moon rotate around the system's combined center of mass, which is positioned inside the earth (see Figure 2.2). The tidal bulges can be seen in Figure 2.1 and an explanation about the centrifugal forces will follow.

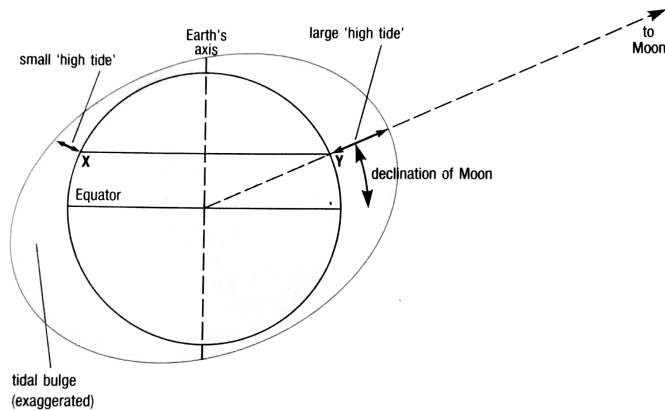


Figure 2.1: The tidal bulges created by the moon. The figure is reproduced from J. Brown (1989)

In the equilibrium model, it is common to examine the absolute acceleration at a fixed point P on the earth's surface, which can be described by Equation 2.1 taken from Myrhaug (2014)

$$\vec{a}_{P,abs} = \vec{a}_{P,rel} + 2\vec{\omega} \times \vec{v}_{P,rel} + \vec{a}_E + \dot{\vec{\omega}} \times \vec{r} + \vec{\omega} \times \vec{\omega} \times \vec{r} \quad (2.1)$$

where $\vec{\omega}$ and $\dot{\vec{\omega}}$ is the earth's angular velocity and acceleration. $\vec{v}_{P,rel}$ and $\vec{a}_{P,rel}$ is the velocity and acceleration of point P seen from the relative frame. \vec{a}_E is the acceleration of the earth's center of mass and \vec{r} is the position vector of point P. Since the point P is fixed to the earth's surface, the two first contributions in Equation 2.1 are equal to zero. The angular acceleration of the earth $\dot{\vec{\omega}}$, is very small, so the term $\dot{\vec{\omega}} \times \vec{r}$ can be neglected. The term $\vec{\omega} \times \vec{\omega} \times \vec{r}$ will always be normal to the earth's axis and will (as long as the earth is considered to be a perfectly round sphere) have the same magnitude on all points on earth. This term will therefore not contribute to the tidal forces, and thus not taken into account. Figure 2.2 shows the earth-moon system with the combined center of mass and point P on the surface of the earth.

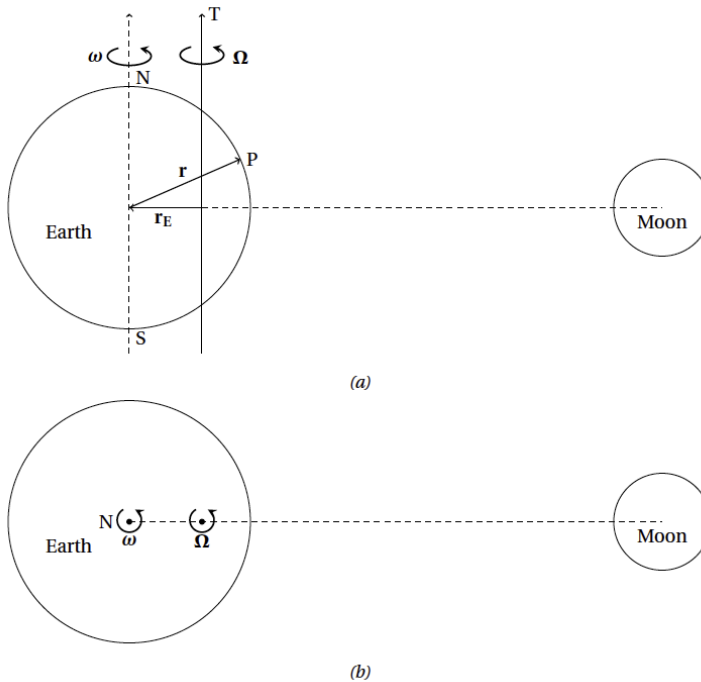


Figure 2.2: Earth-moon system. a) The system with a fixed point P. b) The system seen from above. Figure from Grønningsæter (2015).

The resulting term is then

$$\vec{a}_{P,abs} = \vec{a}_E = \vec{a}_T + \vec{\Omega} \times \vec{\Omega} \times \vec{r}_E \quad (2.2)$$

where $\vec{\Omega}$ is the angular velocity of the earth-moon system (around the axis T), \vec{a}_T is the acceleration of the axis T around the sun and \vec{r}_E is a vector from the earth's center of mass to the earth-moon center of mass. \vec{a}_T is very small because its period is one year, and therefore neglected. The final term can then be written as

$$\vec{a}_{P,abs} = \vec{\Omega} \times \vec{\Omega} \times \vec{r}_E \quad (2.3)$$

The term $\vec{\Omega} \times \vec{\Omega} \times \vec{r}_E$ is the centripetal acceleration due to the rotation of the earth-moon system and is the same for all points on earth as long as the earth is treated as a round sphere.

Inserted in Newtons second law gives

$$\frac{\sum F}{m} = \vec{a}_{P,abs} = \vec{\Omega} \times \vec{\Omega} \times \vec{r}_E \quad (2.4)$$

$$\frac{\sum F}{m} - \vec{\Omega} \times \vec{\Omega} \times \vec{r}_E = 0 \quad (2.5)$$

where m is the mass of a bulge of water. The centripetal acceleration is now considered to be a force which is called the centrifugal force. This force is always pointed away from the moon, and can be written as

$$\vec{S}_0 = -m(\vec{\Omega} \times \vec{\Omega} \times \vec{r}_E) \quad (2.6)$$

The sum of these centrifugal forces is always in balance with the forces caused by the gravitational pull between the earth and the moon, which means that the earth-moon system is in equilibrium. The gravitational force from the moon working on a bulge of water

on earth can be written as

$$\vec{G} = -G \frac{mM}{r^2} \quad (2.7)$$

where G is the gravitational constant, M is the mass of the moon and r is the vector from the moon to the point P . This force is dependent on the distance between the water bulge and the moon, and will consequently depend on the location of point P . When the distance between m and M is large (when the bulge of water is on the far side of the earth) centrifugal forces will dominate, while the side closest to the moon will be dominated by the gravitational pull from the moon as seen in Figure 2.3. These centrifugal forces are the reason why there exists two low and high tides during a period of 24 hours and 50 minutes.

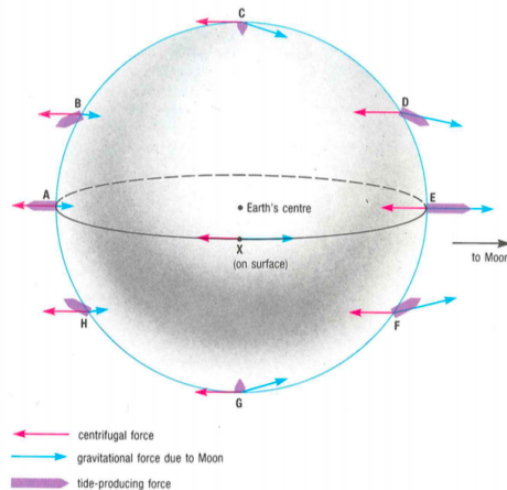


Figure 2.3: Tide producing forces: gravitational forces and centrifugal forces on the earth because of the moon. Figure from J. Brown (1989).

2.1.1 Combined Lunar and Solar Tides

Even though the gravitational pull from the sun working on the earth is only 0.46 times the pull from the moon, it will still have an impact on the tides on earth. The sun also creates two tidal bulges on earth by the same principle as the earth-moon system. The

period of the earth-moon system's rotation around the sun is different from the rotation of the earth-moon system itself. Therefore, the tidal bulges created by the moon and the sun will appear in an oscillatory way. For simplicity however, both the declination of the earth-sun system and the earth-moon system is neglected in the equilibrium model.

Figure 2.4 shows a representation of the earth-moon-sun system in different alignments. When the moon is full or new (the earth, moon and sun is in line) the tidal bulges from the sun and moon is working in the same direction. The high tide will therefore be larger than average, and the low tide will be lower than average. When the moon is in its first or last quarter, the tidal bulge from the sun and moon works normal on each other, resulting in a smaller difference between high and low tide.

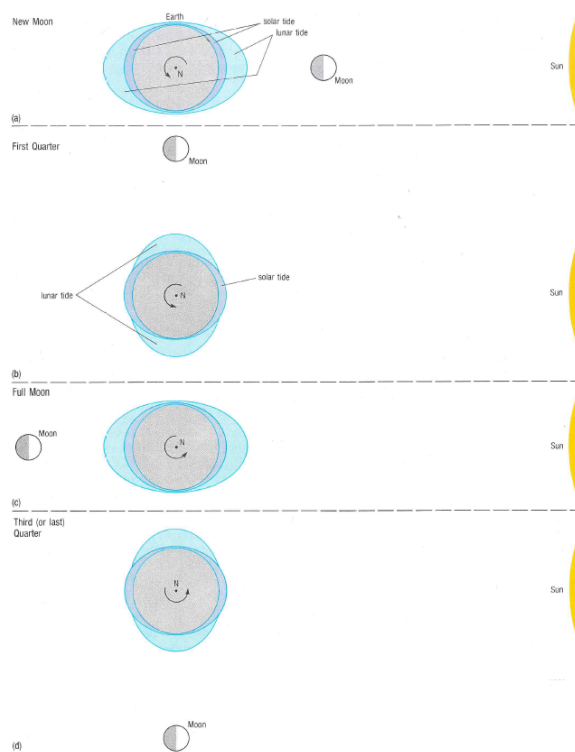


Figure 2.4: The earth-moon-sun system. Figure from J. Brown (1989).

2.2 The Coriolis Effect

In Chapter 2.1, the equilibrium model of tides was explained by use of a fixed point P on the surface of the earth. This resulted in a simplification of Equation 2.1 to Equation 2.3, where only the terms that were influenced by that fixed point remained. Now, consider that the point P is a fluid particle in a current that starts accelerating with an acceleration $\vec{a}_{p,rel}$. The point will now be affected by the earth's rotation, resulting in an effect called the Coriolis effect. Equation 2.1 from Chapter 2.1 can now be written as

$$\vec{a}_{p,abs} \approx \vec{a}_{p,rel} + 2\vec{\omega} \times \vec{v}_{p,rel} \quad (2.8)$$

where $2\vec{\omega} \times \vec{v}_{p,rel}$ is the Coriolis acceleration of a particle P moving with velocity $\vec{v}_{p,rel}$ in a relative reference system with an angular velocity $\vec{\omega}$ (Myrhaug, 2001). Implemented in Newton's second law gives the equation

$$\frac{\vec{F}}{m} = \vec{a}_{abs} = \vec{a}_{rel} + \vec{v}_{p,rel} \quad (2.9)$$

which also can be written as

$$\frac{\vec{F}}{m} - 2\vec{\omega} \times \vec{v}_{p,rel} = \vec{a}_{p,rel} \quad (2.10)$$

From the earth, the term $-2\vec{\omega} \times \vec{v}_{p,rel}$ is experienced as a force, and is the Coriolis force. Because of the Coriolis force, objects will deflect to the right in the northern hemisphere and to the left in the southern hemisphere as seen in Figure 6.1. The magnitude of the force will be at its maximum at the poles, and can be neglected at the equator (Myrhaug, 2001). The Coriolis effect is an important phenomenon in the field of oceanography and meteorology and has a large impact on how the tides and currents behave in the oceans.

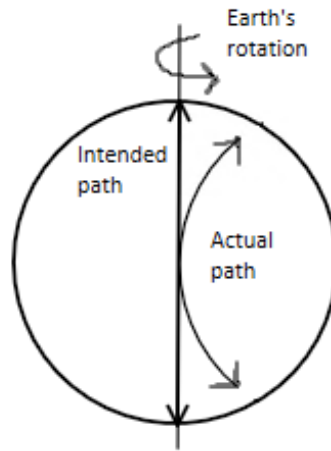


Figure 2.5: Coriolis effect

2.3 The Dynamic model of Tides

The Equilibrium model of tides in Chapter 2.1 is a very simplified, but still a very useful model to describe the tides produced by the moon and sun. However, the effects from continents on earth have been neglected, and these needs to be added to a more detailed model in order to get an accurate description of the tides on earth. The Coriolis effect will also have an impact on the tides. This leads to the more advanced model known as the dynamic model of tides (Pinet, 2015).

The general idea behind the dynamic model is that the tides react actively to the tide generating forces. We start with one hypothetical ocean basin in the northern hemisphere as seen in Figure 2.6. In the first case, the moon is stationed at the west side of the basin, which will cause a tidal wave towards the western shore. This will result in a pressure gradient, which will force the water back to the east. Because of the Coriolis effect, the water will deflect to the right on the way back and force the water to the southern side of the basin, as seen in case 2. Again, the pressure gradient from the southern shore will force the water from the shore. The flow will again deflect to the right because of the Coriolis effect. This rotating flow continues around the basin and will result in a rotary

wave. This rotary wave will rotate around an amphidromic point in an amphidromic system. The amphidromic point will be stationary, which means that it will not have any change in elevation due to high or low tides. This cycle repeats itself every tidal period, which is every 12.42 hours (Garrison, 2007).

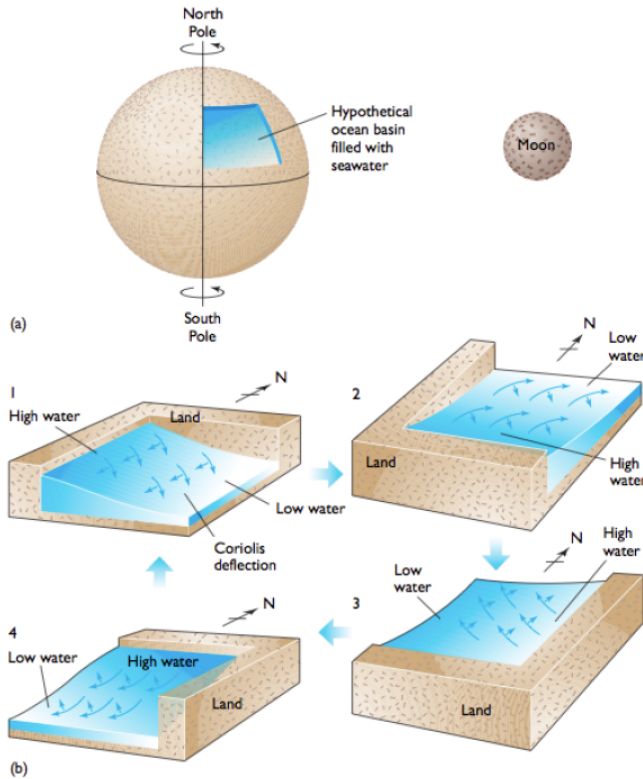


Figure 2.6: The principle behind the dynamic model of tides. Figure from Pinet (2015).

Figure 2.7 shows three amphidromic systems in the North sea. The red lines are called co-tidal lines. The tidal wave crest occurs at the same time for all points on these lines. The blue lines are called co-range lines, where all points on these lines have the same tidal range (elevation) (J. Brown, 1989). As seen, the variation in tides at the eastern coast of Great Britain and in the English Channel, are much larger than at the western coast of Norway near Stavanger.

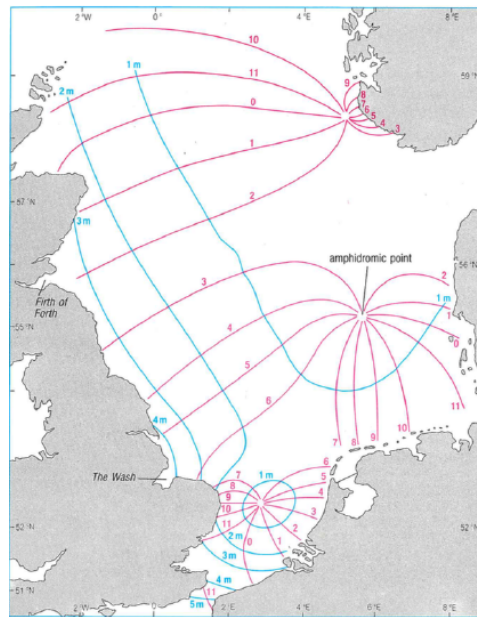


Figure 2.7: Amphidromic systems in the North Sea. Figure from J. Brown (1989).

2.4 Tidal Currents

As mentioned in Chapter 2.3, the tidal motion around an amphidromic point forms a rotary wave. From wave theory, it is known that fluid particles underneath waves move in an orbit. In deep waters, these fluid particles rotate as perfectly round circles, while in finite waters, the fluid particles rotate in an ellipse as seen in Figure 2.8. These orbital motions will decrease further down in the water column and goes to zero at approximately half a wavelength. In shallow waters, the water particles will influence the flow throughout the full water column.

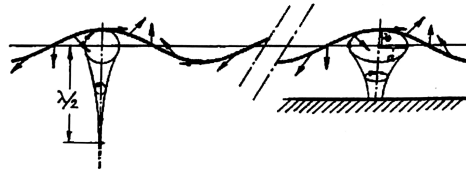


Figure 2.8: Fluid particles underneath a wave in deep (left) and finite water depth (right). Figure from Pettersen (2004).

Because of the large wavelength of a tidal wave compared to the water depth, the water particles will mainly have horizontal motions (u , v). In open oceans where there are no effects from landmasses, the currents will rotate because of the Coriolis effect. If we plot the velocity vectors of a fluid particle in a tidal current, we will get a pattern where the velocity vectors form an ellipse as seen in Figure 2.9. This is called a current rose (J. Brown, 1989).

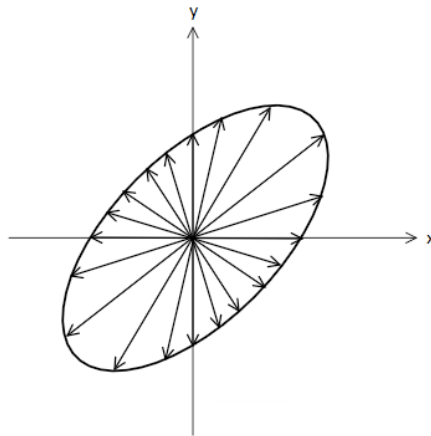


Figure 2.9: Sketch of a current rose. The velocity vectors of a full tidal cycle will form a tidal ellipse. The vectors is plotted 20 times over a tidal cycle.

Sea Environment

Tidal currents are predictable in the sense that they are a direct result of the tidal forces from the moon and sun. Something that is not as easy to predict, is ocean-atmospheric interactions, where wind and waves are of great importance. Both a mean wind and wind gusts will impose a shear stress on the surface and create waves and currents. These waves and currents will together with the tidal currents as well as other factors, create a complex environment that is hard to describe. This chapter will give an introduction to these mechanisms and how they behave in presence of each other.

3.1 Wave Theory

The main source of information in this Section is the Sealoads book by Faltinsen (1990). At first, we assume that the water is incompressible, inviscid and that the fluid motion is irrotational. Under these assumptions, the velocity potential ϕ is useful to describe the velocity vector $\vec{u}(x, y, z, t) = (u, v, w)$ at time t at the point (x, y, z) in a cartesian coordinate system fixed in space. The velocity potential should satisfy the continuity equation $\nabla \cdot \vec{u} = \nabla \cdot (\nabla\phi) = 0$ since the fluid is incompressible. The velocity vector can then be written as

$$\vec{u} = \nabla\phi \equiv \hat{i} \frac{\partial\phi}{\partial x} + \hat{j} \frac{\partial\phi}{\partial y} + \hat{k} \frac{\partial\phi}{\partial z} \quad (3.1)$$

where $(\hat{i}, \hat{j}, \hat{k})$ is unit vectors along (x,y,z) axes respectively. Since the fluid motion is assumed to be irrotational, the vorticity vector $\vec{\omega} = \nabla \times \vec{u}$ is zero everywhere in the fluid. From the continuity equation, the divergence of a gradient leads to the Laplace equation, thus the velocity potential ϕ needs to fullfill the Laplace equation

$$\nabla^2 \phi = \frac{\partial^2 \phi}{\partial x^2} + \frac{\partial^2 \phi}{\partial y^2} + \frac{\partial^2 \phi}{\partial z^2} = 0 \quad (3.2)$$

everywhere in the fluid. The pressure p follows the Bernoulli equation and can be written as

$$p + \rho g z + \rho \frac{\partial \phi}{\partial t} + \frac{\rho}{2} \vec{u} \cdot \vec{u} = C \quad (3.3)$$

where C is a function of time.

3.1.1 Boundary conditions

To be able to find the velocity potential with given assumptions, the Laplace equation needs to be solved with relevant boundary conditions (BC) on the fluid. These can be divided into kinematic and dynamic boundary conditions for the free surface and kinematic boundary conditions for the sea bottom, as seen in Figure 3.1.

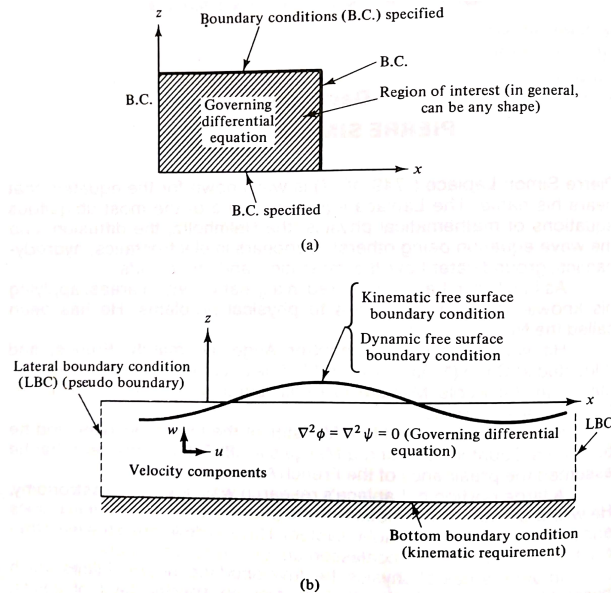


Figure 3.1: a) General structure of a 2D boundary value problem b) 2D water waves specified as a boundary value problem. Figure from Dean and Dalrymple (1991)

Kinematic boundary conditions

Any fixed or moving surface can be expressed mathematically by a function $F(x, y, z, t) = 0$ (Dean and Dalrymple, 1991). The substantial derivative of this function F describes the rate of change with time if we follow a fluid particle in space and can be written as

$$\frac{DF}{Dt} = \frac{\partial F}{\partial t} + \vec{u} \cdot \nabla F \quad (3.4)$$

The free surface can be described by the equation

$$z = \zeta(x, y, t) \quad (3.5)$$

where ζ is the wave elevation. The function F can then be defined as

$$F(x, y, z, t) = z - \zeta(x, y, t) = 0 \quad (3.6)$$

A fluid particle on the free-surface is assumed to always stay on the free-surface. This

means that Equation 3.6 is always satisfied and that Equation 3.4 is equal to zero. The kinematic boundary condition for the free surface thus becomes

$$\frac{\partial}{\partial t}(z - \zeta(x, y, t)) + \nabla\phi \cdot \nabla(z - \zeta(x, y, t)) = 0$$

i.e. (3.7)

$$\frac{\partial\zeta}{\partial t} + \frac{\partial\phi}{\partial x} \frac{\partial\zeta}{\partial x} + \frac{\partial\phi}{\partial y} \frac{\partial\zeta}{\partial y} - \frac{\partial\phi}{\partial z} = 0$$

For a fixed body, such as the sea-bed, the most important boundary conditions that should be defined is the impermeability BC for a fixed body

$$\frac{\partial\phi}{\partial n} = u \cdot n = 0 \quad \text{on the body surface} \quad (3.8)$$

which states that no fluid is entering or leaving the body surface itself. Here, n is the normal vector pointing out of the boundary into the fluid.

Dynamic free surface boundary conditions

Free surfaces like the air-water interface does not support variations in pressure across the interface and must therefore respond in order to maintain uniform pressure (Dean and Dalrymple, 1991). This means that the water pressure is equal to the constant atmospheric pressure. If we choose a constant C , Equation 3.3 can be written as

$$g\zeta + \frac{\partial\phi}{\partial t} + \frac{1}{2} \left(\left(\frac{\partial\phi}{\partial x} \right)^2 + \left(\frac{\partial\phi}{\partial y} \right)^2 + \left(\frac{\partial\phi}{\partial z} \right)^2 \right) = 0 \quad (3.9)$$

on $z = \zeta(x, y, t)$.

Both the free surface conditions from Equation 3.7 and 3.9 are non-linear with a unknown position of the free surface before the equation is solved. However, the conditions can be linearized in order to simplify the problem. Linear wave theory states that velocity potential ϕ is proportional to the wave amplitude if the wave amplitude is small relative

to a characteristic wavelength and body dimensions. The free surface conditions can be transferred from the free surface position $z = \zeta(x, y, t)$ to the mean free surface $z = 0$, and thus the linear form of Equation 3.7 and 3.9 becomes

$$\frac{\partial \zeta}{\partial t} = \frac{\partial \phi}{\partial z} \quad \text{on } z = 0 \text{ (Kinematic condition)} \quad (3.10)$$

$$g\zeta + \frac{\partial \phi}{\partial t} = 0 \quad \text{on } z = 0 \text{ (Dynamic condition)} \quad (3.11)$$

3.2 Nonlinear Wave Effects

A progressive surface wave moving forward will cause water particles underneath the sea surface to start moving in an orbital way as mentioned in Chapter 2.4. If we consider small waves which follows the linear wave theory, the orbital path of the water particles will be closed. However, there often exists waves with different phase velocities and wave lengths in a wave field. When these waves interact, the waves will change from sinusoidal to a nonlinear form with second order effects in terms of ζ_A^2 where ζ_A is the wave amplitude. The fluid particles will now change from a closed path to form a slowly drift in the propagation direction of the wave. As seen in Figure 3.2, these net velocities of the water particles will create a mass transport in the direction of the waves.

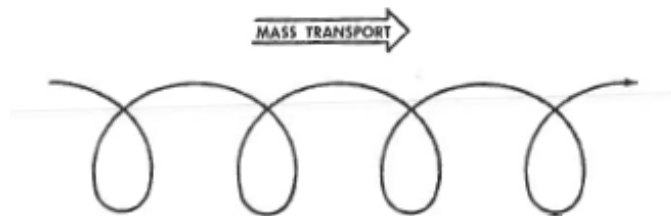


Figure 3.2: Orbital motion of fluid particles inducing mass transport. Figure from Myrhaug (2014).

The oldest and most studied theory for nonlinear waves is the Stokes wave theory, first introduced by Stokes (1846). The theory only works for deep and intermediate water depths, as the solution will break down in shallow water (the solution will not converge).

The characteristics of a Stokes wave is that it has a higher wave crest and a lower (in absolute values) wave trough as seen in Figure 3.3. A Stokes wave also has a wider wave trough and steeper wave crest compared to linear wave theory. The consequence of the nonlinearity in a Stokes wave is that the boundary conditions need to be defined on the actual wave surface, and not on the mean free surface, as for linear wave theory.



Figure 3.3: Comparison of a stokian and linear wave profile. Figure from Myrhaug (2001)

3.3 Wind Induced Currents

When wind is blowing over the ocean surface it will create an ocean surface boundary layer because of friction. A current will then be generated and will decrease further down in the water column. In the Fram expedition towards the North pole from 1893-1896, Fridtjof Nansen experienced that the icebergs did not move in the same direction as the wind, but deflected to the right. Nansen understood that this phenomenon resulted from the rotation of the earth, and asked Vilhelm Bjerknes, who was a professor at Stockholms Högskola for help to solve the problem. Bjerknes forwarded the task to Vagn Walfrid Ekman who was one of his students at the time. Ekman solved the problem in 1902 and the solution is known as the Ekman layer theory.

3.3.1 Ekman Layers

Ekman assumed that the Coriolis effect was central in the problem. Ekman also assumed that the friction forces on the surface because of the wind was directed in the same direction as the wind itself. By use of the Coriolis theory, Ekman found that the water particles deviated to the right of the original direction, something that was in conformity with Nansen's observations. Ekman also found that the different water layers down in the water column each caused a new deviation to the water particles, as well as slowing down the velocity of the water particles because of frictional losses. This is known as the Ekman spiral shown in Figure 3.4.

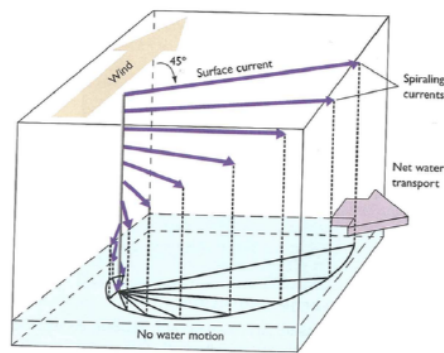


Figure 3.4: The Ekman spiral. Figure from Pinet (2015).

Ekman found that the wind generated currents deviated with an angle of 45° from the original wind direction. This also explained Nansen's iceberg question, because most of the icebergs are located underneath the sea surface and is therefore more affected by the wind generated currents, than by the wind itself (Myrhaug, 2014). Ekman also found that the net mass-transport over the spiral is directed 90° to the right in the northern hemisphere and 90° to the left in the southern hemisphere, known as Ekman transport. This introduces the terms upwelling and downwelling which is two important terms regarding nutrition transport in the oceans (Pinet, 2015).

Ekman spirals does not only exist at the sea surface. In the atmosphere and at the sea floor, there can also exist Ekman spirals. The direction of the deviation will then be directed

opposite ways of the Ekman layers at the seafloor, to the left in the northern hemisphere and to the right in the southern hemisphere (Myrhaug, 2014).

Observations and experiments of the Ekman spiral showed that the real deviation of the water particles was not 45° , but between 5° and 20° . This is because of turbulence in the flow, something that the Ekman model excludes (Cushman-Roisin, 2011).

3.4 Interaction Between Waves and Currents

Waves and currents will interact with each other hydrodynamically. This means that the waves will be influenced in a nonlinear way by the current, and vice versa. Thus, the current and waves creates a intermutual boundary layer that complicates the calculations. In addition, there will be a modification of the phase speed and the wavelength of the waves, leading to refraction of the waves (Soulsby, 1997). Waves propagating in the same direction as a current, will experience increased wavelength and decreased wave height, while waves propagating in the opposing direction as the current, will experience decreased wavelengths and an increased wave height.

Waves, in the presence of a current will impose an extra roughness on the current. This roughness will be in addition to the surface roughness height z_0 that will be described in Chapter 5.3. The extra roughness induced by the waves will lead to increased mixing near the bed, thus the turbulence will increase (Nielsen, 1992). This additional roughness can be included by introducing the apparent roughness coefficient z_a in the logarithmic velocity profile that will be introduced in Chapter 5.3.1. The more wave dominated flow, the larger apparent roughness (Holmedal, Myrhaug, and Rue, 2003).

Apparent roughness is a function of the relative roughness on the sea-bed, wave characteristics, velocity of the current compared to the wave orbital velocity and the angle between the waves and current (Grant and Madsen, 1979). It is therefore multiple factors that have the ability to influence the apparent roughness, and thus the friction in the combined waves and tidal current boundary layer.

Waves in shallow and intermediate waters produce an oscillatory velocity within the wave boundary layer at the sea-bed, where the velocity amplitude increase rapidly with height from zero at the sea-bed. These oscillatory velocities will, in the absence of a current, be within the wave boundary layer on the sea-bed, which can be a few millimeters or centimeters thick. Because of these small scales, where the turbulence is concentrated within the thin wave boundary layer, the waves will have the ability to impose a much larger sea-bed shear stress compared to a pure tidal current. This large sea-bed shear stress have the strength to detach sediments on the sea-bed (Soulsby, 1997). However, as the velocities within the wave boundary layer oscillates, they are an ineffective transport mechanism. The current boundary layer on the other hand, is typically multiple meters in height and is therefore a much better transport mechanism. The current have the ability to transport sediments already detached by the waves. Thus the combined waves and tidal flow will initiate sediment detachment and transport (Grant and Madsen, 1979). Sediment transport is of great importance with regard to forming of river deltas and beaches in coastal areas.

Figure 3.5 shows a representation of the nonlinear interaction between waves and current shear stress with an angle between them. As seen, the maximum shear stress in the combined waves and tidal current have mean direction based on the direction of the pure waves and pure current flow. This change in direction have the ability to change the direction of the flow and thus the direction of the sediment transport.

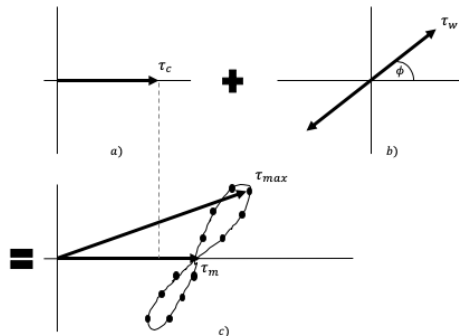


Figure 3.5: Shear stress near the sea-bed for a combined waves and tidal current flow. Figure reproduced from (Soulsby, 1997)

Boundary Layers

A boundary layer is defined as the flow region where the viscous effects are significant (Cengel and Cimbala, 2014). This will result in a change of velocity gradients near the surface and the no-slip condition applies. The no-slip condition states that the velocity of a fluid in motion will decrease as it approaches a surface and will eventually come to a complete stop as long as the surface itself is not moving. There exists both laminar and turbulent boundary layers, depending on the Reynolds number. However, current and wave behavior is generally turbulent, thus the focus will be on turbulent boundary layers in this thesis. Both the boundary layer and the no-slip condition exist because of friction between the fluid and the boundary, which leads to turbulent shear stresses in the fluid which can be written as

$$\tau_{turb} = -\rho \overline{u_i' u_j'} \quad (4.1)$$

This turbulent shear stress is commonly known as Reynolds stresses, and is in much use in many turbulence models such as the Reynolds Averaged Navier Stokes (RANS) solvers. The French mathematician Joseph Boussinesq came up with a formulation of the turbulent shear stress which can be written as

$$\tau_{turb} = \mu \frac{\partial u}{\partial y} \quad (4.2)$$

where μ is the dynamic viscosity of the fluid and $\frac{\partial u}{\partial y}$ is the velocity gradient (Cengel and Cimbala, 2014).

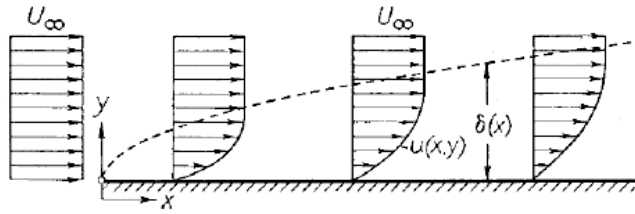


Figure 4.1: Sketch of a laminar boundary layer. Figure from Schlichting and Gersten (2017).

Boundary layers exist in many forms and sizes, as atmospheric boundary layers, ocean surface boundary layers and boundary layers at the sea bottom. What these boundary layers have in common, is that they are developing over an approximately flat terrain. For example, if wind is blowing over a hill or a very rough terrain such as steep waves in the ocean, it is likely that the flow will separate, and vortices will be shed. This will lead to a decomposition of the boundary layer, and the boundary layer equations which will be presented in Chapter 4.1 will not apply. However, for large scale motions where the length scale L is much larger than the height scale H , the boundary layer theory is applicable, which makes it suitable in the prediction of tidal flows, which is typically a large scale motion (Myrhaug, 2014).

4.1 The boundary layer approximation

The boundary layer equations is a simplification of the full Navier Stokes equations. They narrow the step between the Euler equations, which does not follow the no slip condition, and the Navier Stokes equations (Cengel and Cimbala, 2014). The Navier Stokes equations originates from Newton's second law and can (including the Coriolis acceleration) be written as

$$\frac{\partial u}{\partial t} + u \frac{\partial u}{\partial x} + v \frac{\partial u}{\partial y} + w \frac{\partial u}{\partial z} - f_v = -\frac{1}{\rho} \frac{\partial p}{\partial x} + \nu \left(\frac{\partial^2 u}{\partial x^2} + \frac{\partial^2 u}{\partial y^2} + \frac{\partial^2 u}{\partial z^2} \right) \quad (4.3)$$

$$\frac{\partial v}{\partial t} + u \frac{\partial v}{\partial x} + v \frac{\partial v}{\partial y} + w \frac{\partial v}{\partial z} + f_u = -\frac{1}{\rho} \frac{\partial p}{\partial y} + \nu \left(\frac{\partial^2 v}{\partial x^2} + \frac{\partial^2 v}{\partial y^2} + \frac{\partial^2 v}{\partial z^2} \right) \quad (4.4)$$

$$\frac{\partial w}{\partial t} + u \frac{\partial w}{\partial x} + v \frac{\partial w}{\partial y} + w \frac{\partial w}{\partial z} - g = -\frac{1}{\rho} \frac{\partial p}{\partial z} + \nu \left(\frac{\partial^2 w}{\partial x^2} + \frac{\partial^2 w}{\partial y^2} + \frac{\partial^2 w}{\partial z^2} \right) \quad (4.5)$$

where $\{u, v, w\}$ is the velocities in $\{x, y, z\}$ direction respectively, p is the pressure, $\{f_u, f_v\}$ is the effect from the Coriolis acceleration, ν is the fluid kinematic viscosity, ρ is the fluid density and g is the gravitational acceleration. Now, consider a boundary layer with height δ and length L . For boundary layers, the height δ is much smaller than the length L ($\delta \ll L$) and can therefore be modeled as a thin layer compared to the flow region. Because of the mentioned no slip condition, the velocity at the wall is zero, and approaching the free stream velocity U_0 away from the wall. Because the boundary layer is a thin layer, the velocity goes from 0 to U_0 within a short period of time. Consequently, the vertical velocity gradient $\frac{\partial U}{\partial z}$ is large. For the boundary layer to remain thin and thus comply with the continuity equation, the vertical velocity W must be much smaller than the horizontal velocity component, such that $W \ll U$ is valid. By use of this dominating balance and scaling laws, the Navier Stokes equations can be written as

$$\frac{\partial u}{\partial t} + u \frac{\partial u}{\partial x} + v \frac{\partial u}{\partial y} + w \frac{\partial u}{\partial z} - f_v = -\frac{1}{\rho} \frac{\partial p}{\partial x} + \nu \frac{\partial^2 u}{\partial z^2} \quad (4.6)$$

$$\frac{\partial v}{\partial t} + u \frac{\partial v}{\partial x} + v \frac{\partial v}{\partial y} + w \frac{\partial v}{\partial z} + f_u = -\frac{1}{\rho} \frac{\partial p}{\partial y} + \nu \frac{\partial^2 v}{\partial z^2} \quad (4.7)$$

$$\frac{\partial p}{\partial z} = -\rho g \quad (4.8)$$

These three equations are known as the boundary layer equations. Equation 4.8 states that there is no change in the pressure in the z -direction throughout the boundary layer, which is an important assumption then solving the boundary layer equations.

4.2 The low Rossby number approximation

The Rossby number is an important parameter when we want to determine whether the motion in the oceans are dominated by inertia or Coriolis forces. Surface waves made from wind are typically inertia dominated, because of the large mass they contain, but ocean tides are large scale motions which are typically Coriolis dominated, because of extremely long wave-lengths. The Rossby number is defined by

$$R_0 = \frac{U_0}{Lf_0} \quad (4.9)$$

where U_0 is the free stream velocity, L is the characteristic length of the motion and f_0 the Coriolis paramter at the given latitude. U_0 is known as the acceleration (Inertia) term, and Lf_0 is known as the Coriolis term. It can be seen that for large Rossby numbers, the acceleration term is dominant, and for small Rossby numbers, the Coriolis term is dominant. As mentioned, large scale motions such as ocean tides is typically Coriolis dominant because of the very large length scale L , which again leads to low Rossby numbers. We can then use the so called low Rossby number approximation to neglect all the advective terms. Thus, the boundary layer Equations 4.6, 4.7 and 4.8 can be simplified and written as

$$\frac{\partial u}{\partial t} = -\frac{1}{\rho} \frac{\partial p}{\partial x} + \nu \frac{\partial^2 u}{\partial z^2} + f_v \quad (4.10)$$

$$\frac{\partial v}{\partial t} = -\frac{1}{\rho} \frac{\partial p}{\partial y} + \nu \frac{\partial^2 v}{\partial z^2} - f_u \quad (4.11)$$

$$\frac{\partial p}{\partial z} = -\rho g \quad (\text{unaffected}) \quad (4.12)$$

Turbulence and Turbulence Modeling

5.1 The Reynolds Model

The Navier Stokes equations describes a viscous incompressible fluid flow, and can (with Einstein's summation convention) be written as

$$\frac{\partial u_i}{\partial t} + \frac{\partial}{\partial x_j}(u_i u_j) = -\frac{1}{\rho} \frac{\partial p}{\partial x_i} + \nu \frac{\partial^2 u_i}{\partial x_j \partial x_j} \quad (5.1)$$

$$\frac{\partial u_i}{\partial x_i} = 0 \quad (5.2)$$

where u_i is the fluid velocity where $i = \{1, 2, 3\} = \{x, y, z\}$ respectively (Alfonso, 1993). The Navier Stokes (NS) equation is very time consuming and computational demanding to solve by direct numerical simulations (DNS). Osborne Reynolds came therefore up with a decomposing of the NS equations. The dependent variables (u and p) in Equation 5.1 and 5.2 are decomposed into mean and fluctuating parts

$$u(x_i, t) = \overline{u(x_i, t)} + u'(x_i, t) \quad (5.3)$$

$$p(x_i, t) = \overline{p(x_i, t)} + p'(x_i, t) \quad (5.4)$$

where $\overline{u(x_i, t)}$ represents the mean turbulent velocity field and $u'(x_i, t)$ represents the fluctuating velocity field. Substituting Equation 5.3 and 5.4 into the Navier Stokes equation, leads to the Reynolds Averaged Navier Stokes (RANS) equation

$$\frac{\partial \overline{u_i}}{\partial t} + \frac{\partial \overline{u_i u_j}}{\partial x_j} = -\frac{1}{\rho} \frac{\partial \overline{p}}{\partial x_i} + \nu \frac{\partial^2 \overline{u_i}}{\partial x_j \partial x_j} - \frac{\partial \overline{u_i' u_j'}}{\partial x_j} \quad (5.5)$$

$$\frac{\partial \overline{u_i}}{\partial x_i} = 0 \quad (5.6)$$

The term $\overline{u_i' u_j'}$ in Equation 5.5 is the Reynolds stresses, as presented in Equation 4.1. These stresses must be modeled by use of various turbulence models (Holmedal, 2002).

5.2 The Generalized Eddy Viscosity Concept

To be able to solve the RANS equation (Equation 5.5) we need to be able to model the Reynolds stresses. The main idea on how to do this is to define a relationship between the velocity field and the shear stresses in the fluid (Nielsen, 1992). This can be done in various ways, but a common approach is the eddy viscosity concept, also known as the generalized eddy viscosity hypothesis. The main principle behind the generalized eddy viscosity concept is to configure the RANS equation such that it becomes identical to the laminar Navier Stokes equations (Holmedal, 2002). Generalized eddy viscosity can be written on the form

$$-\overline{u_i' u_j'} = \nu_T \left(\frac{\partial \overline{u_i}}{\partial x_j} + \frac{\partial \overline{u_j}}{\partial x_i} \right) - \frac{2}{3} k \delta_{ij} \quad (5.7)$$

where δ_{ij} is the Kronecker delta function and ν_T is the eddy viscosity. The turbulent kinetic energy, k can be written as

$$k = \frac{1}{2} \overline{u_i' u_j'} \quad (5.8)$$

The eddy viscosity ν_T is unknown and needs to be determined to be able to use the model in a practical way. The eddy viscosity must be modeled as a function of the average flow variables (Cengel and Cimbala, 2014). Depending on how this is done, our model will be either a zero, one or two-equation model with different accuracy.

Ludwig Prandtl developed in the early 20th century a model which is called the Prandtl lifting length model. Prandtl assumed that the eddy viscosity could be written as

$$\nu_T = l_m V_m \quad (5.9)$$

where l_m is the mixing length and V_m is the velocity scale of the largest turbulent eddies. Prandtl found that V_m is proportional to the velocity gradient ($\frac{\partial \bar{u}}{\partial z}$) times the mixing length (l_m) and the eddy viscosity can then be written as

$$\nu_T = l_m^2 \left| \frac{\partial \bar{u}}{\partial z} \right| \quad (5.10)$$

Prandtl described the mixing length model (which is a zero equation model) to be "only a rough approximation" of the turbulent shear stresses. The model have however been regarded as a successful model to describe the eddy viscosity in a fluid. Today, the mixing length model is however regarded to not be sufficient in terms of describing the eddy viscosity because the model is based on the assumption that the turbulent eddies interacts in the same way as molecules in a gas. This have been concluded not to be the case, and the mixing length model is therefore not in much use today (Holmedal, 2002).

To be able to model the eddy viscosity in an accurate way, a model which describes the transport of the turbulent length and velocity scale in Equation 5.9 is needed. Prandtl and Kolmogorov suggested to replace the velocity scale of the largest turbulent eddies (V_m) with the square root of the turbulent kinetic energy and define these to be proportional with

each other. This is known as the Kolmogorov-Prandtl relation and can be written as

$$\nu_T = C_\mu \sqrt{k} l_m \quad (5.11)$$

where C_μ is an empirical constant.

The Kolmogorov-Richardson cascade (see Richardson, 1965) states that for turbulent flows, the viscous forces in the flow extracts the kinetic energy from the turbulence and transforms it into heat. The energy is first transferred from the high-energy eddies (large eddies) to the low-energy eddies (small eddies) before it eventually dissipates. The viscous effects are therefore negligible for large eddies. The dissipation rate of turbulent kinetic energy can therefore be determined from the turbulent length l_m and the velocity scales of the largest eddies V_m . From dimensional analysis, the dissipation term can be modeled as $\epsilon = V_m^3 / l_m$ where $V_m \sim \sqrt{k}$ (Holmedal, 2002). This leads to the viscous dissipation rate of turbulent kinetic energy ϵ and can be written as

$$\epsilon = C_D \frac{k^{3/2}}{l_m} \quad (5.12)$$

where C_D is an empirical constant (Holmedal, 2002).

In order to describe the turbulence as realistic as possible, we need transport equations for both the turbulent length L and the velocity scale V_m . This leads to two-equation turbulence models which exists in various versions. One of the most common two-equation turbulence models in use today is the $k - \epsilon$ turbulence model which can be written as

$$\nu_T = C_D C_\mu \frac{k^2}{\epsilon} \equiv c_1 \frac{k^2}{\epsilon} \quad (5.13)$$

where the empirical constants C_D, C_μ can be described by the empirical constant c_1 . The transport equation for ϵ can now be found from the Navier Stokes equations. The $k - \epsilon$ model can now be written as

$$\frac{\partial k}{\partial t} + \bar{u}_j \frac{\partial k}{\partial x_j} = \frac{\partial}{\partial x_j} \left(\frac{\nu_T}{\sigma_k} \frac{\partial k}{\partial x_j} \right) + \nu_T \left(\frac{\partial \bar{u}_i}{\partial x_j} + \frac{\partial \bar{u}_j}{\partial x_i} \right) \frac{\partial \bar{u}_i}{\partial x_j} - \epsilon \quad (5.14)$$

$$\frac{\partial \epsilon}{\partial t} + \bar{u}_j \frac{\partial \epsilon}{\partial x_j} = \frac{\partial}{\partial x_j} \left(\frac{\nu_T}{\sigma_\epsilon} \frac{\partial \epsilon}{\partial x_j} \right) + c_{1\epsilon} \frac{\epsilon}{k} \nu_T \left(\frac{\partial \bar{u}_i}{\partial x_j} + \frac{\partial \bar{u}_j}{\partial x_i} \right) \frac{\partial \bar{u}_i}{\partial x_j} - c_{2\epsilon} \frac{\epsilon^2}{k} \quad (5.15)$$

where c_1 , σ_k , σ_ϵ , $c_{1\epsilon}$ and $c_{2\epsilon}$ is constants that needs to be determined experimentally. The $k - \epsilon$ model must be solved at the same time as the RANS equations (Equation 5.5) (Holmedal, 2002).

5.3 The Impact of Bottom Roughness

Basic fluid turbulent models tend to start with flow over a flat plate for simplicity. However, most of the seafloor is covered by sedimentary structures such as dunes and ripples, which will add a roughness to the surface. These small structures do not influence the main flow over a surface, but they have a large impact on the boundary layer and turbulence close to the seabed, because of added friction (Nielsen, 1992). The friction coefficient is a common parameter to estimate the frictional resistance on the seabed. For laminar flow, the friction coefficient only depends on the Reynolds number. For turbulent flow, the surface roughness has an impact on the friction coefficient and in fully rough and turbulent flows, the friction coefficient is independent of the Reynolds number and is only a function of surface roughness (Cengel and Cimbala, 2014).

To be able to make models of the seabed roughness with acceptable accuracy, we need to be able to describe the seabed shear stress. This can be done either by describing the seabed geometry by use of the Nikuradse grain roughness k_s (also called the hydraulic roughness), or by the roughness height z_0 which can be derived from Equation 5.19. Nikuradse found that for fully turbulent/hydrodynamically rough flows, the logarithmic velocity profile (see Chapter 5.3.1) over packed sand grains with diameter d went to zero at roughness length equal to

$$z_0 = \frac{1}{30}d \quad (5.16)$$

where d is the diameter of a sand grain. The relationship between the roughness length

and the Nikuradse roughness thus becomes

$$k_s = 30z_0 \quad (5.17)$$

Implemented in the Reynolds number leads to the Reynolds roughness number

$$R_r = \frac{U_* z_0}{\nu} \quad (5.18)$$

where U_* is the turbulent velocity at the sea-bed (see Equation 5.20) and ν is the kinematic viscosity. It is clear that lower sea-bed shear stress leads to lower Reynolds numbers and thus more laminar flow (Soulsby, 1997).

5.3.1 Universal Law of The Wall

From experiments, the velocity profile of a steady, uniform and turbulent boundary layer tends to approach a logarithmic profile. The velocity can therefore be described by the logarithmic velocity law called the law of the wall which can be described by

$$\frac{\bar{u}(z)}{\bar{u}_*} = \frac{1}{\kappa} \ln \frac{z}{z_0} \quad (5.19)$$

$$\bar{u}_* = \sqrt{\frac{\tau(0)}{\rho}} \quad (5.20)$$

where $\tau(0)$ is the sea bed shear stress, z is a finite elevation above the sea bed and κ is the Von Karman's constant (usually 0.4). Note that this velocity profile is not a good approximation for bottom flow which is influenced by the boundary layer from the water surface and is therefore, according to Nielsen (1992), only applicable for the bottom 20-30 % of the water column.

Model Formulation

6.1 Governing Equations

We consider a flow over a flat bottom with no interfering land masses. The cartesian coordinate system is placed at the bottom with positive x direction to the east, y to the north and z describes the vertical distance from the bottom to the sea surface. As mentioned in Chapter 4.1, the vertical velocity w is much smaller than the horizontal velocity component u within a boundary layer, as long as the bottom is flat. By combining the boundary layer approximation from Chapter 4.1 and the low Rossby number approximation from Chapter 4.2 where all the advective terms can be neglected because of the assumption of horizontal uniform flow, we can simplify the RANS equations mentioned in Chapter 5.1 to

$$\frac{\partial u}{\partial t} = -\frac{1}{\rho} \frac{\partial p}{\partial x} + \frac{\partial}{\partial z} \left(\nu_T \frac{\partial u}{\partial z} \right) + f v \tag{6.1}$$

$$\frac{\partial v}{\partial t} = -\frac{1}{\rho} \frac{\partial p}{\partial y} + \frac{\partial}{\partial z} \left(\nu_T \frac{\partial v}{\partial z} \right) - f u \tag{6.2}$$

where u and v are the horizontal velocities and f is the Coriolis parameter. Note that the Coriolis effect does not come into account in the modeling of only waves, i.e. the terms f_v and f_u is then excluded from the equations.

Again, By use of the boundary layer approximation, and with the advective terms neglected, the transport equations for k and ϵ in the k - ϵ turbulence closure model can be

written as (See Rodi, 1993)

$$\frac{\partial k}{\partial t} = \frac{\partial}{\partial z} \left(\frac{\nu_T}{\sigma_k} \frac{\partial k}{\partial z} \right) + \nu_T \left(\left(\frac{\partial u}{\partial z} \right)^2 + \left(\frac{\partial v}{\partial z} \right)^2 \right) - \epsilon \quad (6.3)$$

$$\frac{\partial \epsilon}{\partial t} = \frac{\partial}{\partial z} \left(\frac{\nu_T}{\sigma_\epsilon} \frac{\partial \epsilon}{\partial z} \right) + C_{\epsilon 1} \frac{\epsilon}{k} \nu_T \left(\left(\frac{\partial u}{\partial z} \right)^2 + \left(\frac{\partial v}{\partial z} \right)^2 \right) - C_{\epsilon 2} \frac{\epsilon^2}{k} \quad (6.4)$$

where the standard values for the empirical constants is $\{c_1, c_{\epsilon 1}, c_{\epsilon 2}, \sigma_k, \sigma_\epsilon\} = \{0.09, 1.44, 1.92, 1.0, 1.3\}$.

The direction of the waves is constant and in the x direction. The direction of the current varies with the tidal cycle and consists of u and v components. See also Figure 2.9 in Chapter 2.4.

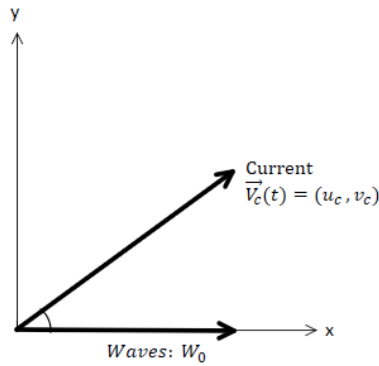


Figure 6.1: Sketch showing the direction of the current and the waves

6.2 Boundary Conditions

6.2.1 At the bottom

The velocity at the sea-bed is defined by the no slip condition mentioned in Chapter 4

$$(u, v) = (0, 0) \quad \text{at} \quad z = z_0 \quad (6.5)$$

The sea-bed is assumed to be hydraulically rough (see Chapter 5.3), hence, the roughness at the sea-bed is defined by the Nikuradse roughness k_s , given by Equation 5.17. Rodi (1993) assumed equilibrium between the production and dissipation of turbulence, hence the boundary conditions for the turbulent kinetic energy, k and dissipation, ϵ at the sea bed can be written as

$$k = \nu_T \sqrt{\frac{\left(\frac{\partial u}{\partial z}\right)^2 + \left(\frac{\partial v}{\partial z}\right)^2}{c_1}} \quad (6.6)$$

$$\epsilon = c_1^{3/4} \frac{k^{3/4}}{\kappa z_0} \quad (6.7)$$

where $\kappa = 0.4$. Both these boundary conditions is evaluated at the first node from the bottom.

6.2.2 At the outer boundary

Pure tidally driven flow

As previously mentioned, a tidal wave has a wavelength far greater than amplitude ($\lambda \gg \zeta_A$). This defines waves with very low steepness which means that linear wave theory can be used (Pettersen, 2004). It is therefore sufficient to use the mean free surface rather than the free surface itself as outer boundary for the pure tidally driven flow (Holmedal and Myrhaug, 2013). Holmedal and Myrhaug (2013) assumed no shear stress at the sea

surface. The boundary conditions becomes

$$\frac{\partial u}{\partial z} = 0 \quad (6.8)$$

$$\frac{\partial v}{\partial z} = 0 \quad (6.9)$$

There is no flux for the turbulent quantities, the boundary conditions thus becomes

$$\frac{\partial k}{\partial z} = 0 \quad (6.10)$$

$$\frac{\partial \epsilon}{\partial z} = 0 \quad (6.11)$$

Regular waves alone

For regular waves alone, the upper edge of the flow domain, $z = z_{max}$, is chosen, such that the boundary layer effects have disappeared (Holmedal, Myrhaug, and Rue, 2003). The Neumann condition is applied for the velocity, such that Equation 6.8 holds. There is still no flux for the turbulent quantities, such that Equation 6.10 and 6.11 holds.

Because of no turbulent quantities, the velocity will approach the free stream velocity amplitude W . The solution must be periodic with the period of oscillation, thus, the free stream velocity variation is sinusoidal and given by

$$W_0 = W \sin(\omega t) \quad (6.12)$$

where ω is the angular frequency of oscillation.

Combined waves and tidal flow

The velocity components for waves plus current at $z = z_{max}$ is given as

$$u = W_0 + U_c(t) \quad (6.13)$$

$$v = V_c(t) \quad (6.14)$$

where U_c and V_c is the mean current velocity in x and y direction respectively. Zero

flux conditions for the turbulent quantities still applies, thus Equation 6.10 and 6.11 is valid. The application of zero flux for the turbulent quantities is discussed by Holmedal, Myrhaug, and Rue (2003), and will give a unrealistic representation for k and ϵ close to the outer boundary. This is because the eddy viscosity will have a zero vertical gradient at the outer boundary z_{max} . However, because of the small vertical velocity gradients close to the outer boundary, the velocities are not much affected by the inaccurate velocity. Because of the correct velocities over the entire flow domain, the turbulent quantities will be correct modeled further away from the outer boundary, and will give a correct representation of the boundary layer close to the sea-bed as is the main interest in present work (Holmedal, Myrhaug, and Rue, 2003).

6.3 Forcing Function

Pure tidally driven flow

Since the boundary layer approximation is valid, the horizontal pressure gradients are considered to be constant throughout the boundary layer. The horizontal pressure gradients are therefore assumed to be in equilibrium with the local accelerations and the Coriolis terms in the free stream velocities U_0 and V_0 . Equation 6.1 and 6.2 thus becomes

$$-\frac{1}{\rho} \frac{\partial p}{\partial x} = \frac{\partial U_0}{\partial t} - fV_0 \quad (6.15)$$

$$-\frac{1}{\rho} \frac{\partial p}{\partial y} = \frac{\partial V_0}{\partial t} + fU_0 \quad (6.16)$$

Combined waves and tidal flow

The boundary layer approximation still yields, such that the horizontal pressure gradients are constant throughout the boundary layer. The horizontal pressure gradient can therefore be taken from the free stream velocity variation W_0 close to sea-bed. The forcing function thus becomes

$$-\frac{1}{\rho} \frac{\partial p}{\partial x} = \frac{\partial W_0}{\partial t} - \frac{1}{\rho} \frac{\partial p_c}{\partial x} \quad (6.17)$$

$$-\frac{1}{\rho} \frac{\partial p}{\partial y} = -\frac{1}{\rho} \frac{\partial p_c}{\partial y} \quad (6.18)$$

Here $\frac{\partial p_c}{\partial x}$ and $\frac{\partial p_c}{\partial y}$ represents the constant horizontal pressure gradients due to the current. For conditions where the components from the wave is dominating, this pressure gradient becomes at least two orders of magnitude smaller than the pressure gradient from the waves itself, and can therefore be neglected for wave dominated situations (A. Davies et al., 1988). Note that W_0 is only represented in the horizontal pressure gradient in the x direction, because the direction of the waves is always in the x direction.

6.4 Numerical method

The four governing equations presented in Chapter 6.1, respectively for u, v, k and ϵ is solved using a finite difference method as described by Holmedal and Myrhaug (2013). The most interesting areas in the flow domain are close to the sea bed. Geometric stretching of the mesh was therefore conducted to get a finer resolution close to the sea-bed. In order to solve the four equations, time integration is needed. This is done simultaneously for all the equations by the integrator VODE (P. N. Brown et al., 1989).

Verification of the Model for Regular Waves Alone

The model for regular waves alone, was applied by Justesen (1991) to find turbulent quantities in the wave boundary layer under sinusoidal waves alone. The model is a standard one dimensional two-equation $k - \epsilon$ model with governing equations and boundary conditions as described in Chapter 6. The results have been modeled with a A/k_N value of 3700 where A is the particle amplitude in the free-stream oscillation. The results in this chapter is compared to experimental laboratory measurements from test number 13 performed by Jensen et al. (1989). Test number 13 showed to give the most detailed measurements of the rough turbulent boundary layer.

Figure 7.1 shows the modeled velocity profiles compared to the measurements from test number 13 for both the acceleration phase (Figure 7.1a) and the deceleration phase (Figure 7.1b) in the logarithmic scale. As seen, the velocity profiles exhibit the characteristic overshoot and that the velocity follows the logarithmic law close to the sea-bed. It can also be seen that there is a clear difference between the acceleration phase and the deceleration phase.

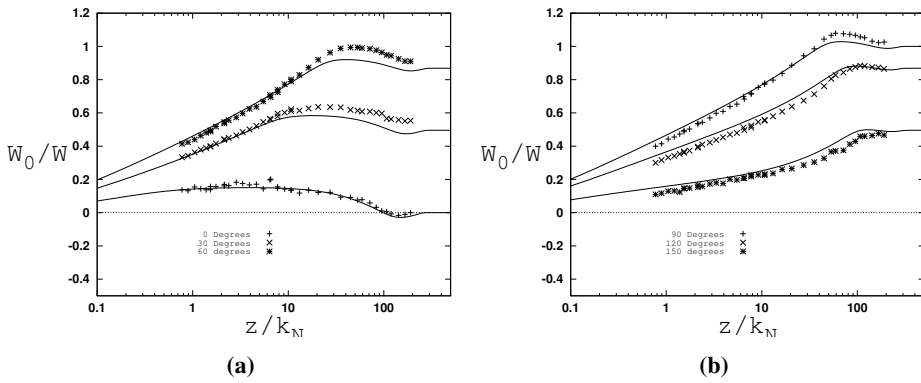


Figure 7.1: Comparison between modeled (lines) and measured (dotted lines) velocity profiles

Figure 7.2 shows a representation of the turbulent kinetic energy at four phases during a half circle. As seen, the modeled results are slightly under-predicted compared to the measurements.

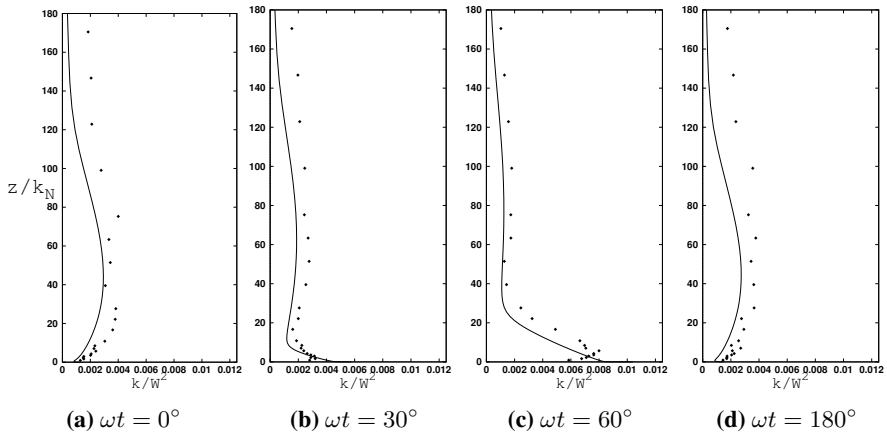


Figure 7.2: Comparison between modeled (lines) and measured (dotted lines) profiles of turbulent kinetic energy

Figure 7.3 represents the Reynolds shear stress. As seen, there is a good agreement between the modeled and measured values.

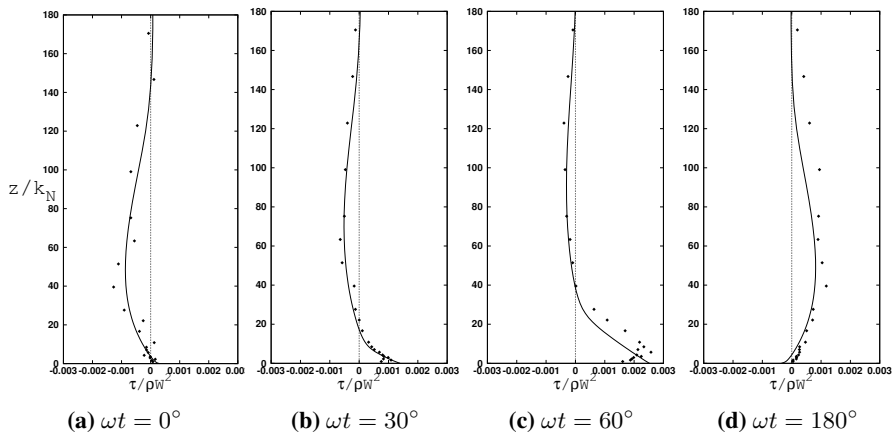


Figure 7.3: Comparison between modeled (lines) and measured (dotted lines) Reynolds shear stress profiles

Figure 7.4 shows a comparison between modeled and measured friction velocity plotted against the phase variable ωt in one wave cycle. The measured friction velocity has been obtained from a 'log-fit' to the near-bed measured velocity component. Close to the flow reversal (zero-crossing), the friction velocity becomes inaccurate. This is because of the assumption that there exists an equilibrium between the production and dissipation of turbulent kinetic energy. The logarithmic law will therefore break down and no measured results can be shown for this area (Holmedal, Myrhaug, and Rue, 2003).

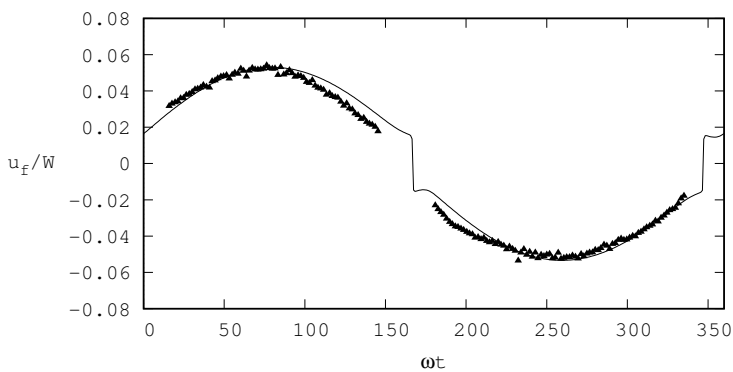


Figure 7.4: Comparison between predicted (lines) and measured (dotted lines) friction velocity

Results and Discussion

In this chapter, results from the combined waves and tidal current model will be presented and discussed. The sinusoidal waves have an amplitude of 0.92 meters on the sea-surface and a period of 6 seconds. The outer boundary for the combined model is 25 cm above the sea-bed. Pure tidal flow has been modeled with a Coriolis parameter of $f = 1.112 * 10^{-4}$ and the total tidal period is 12.25 hours. The total water depth of the pure tidal flow is 120 meters with a free stream velocity taken at 70m, as these velocities showed to be least affected by the sea-bed and sea-surface. Particle trajectory ellipses have been modeled for different heights above the sea-bed and plotted against the ellipses for pure tidal current for comparison. The ellipses follow a clockwise rotation. Simulations have been performed with two different values of roughness height to be able to determine the importance of bottom roughness. These values is $z_0 = 0.1$ cm and 0.01 cm respectively. According to table 4 in Soulsby (1997), a roughness height of 0.1 cm corresponds to coarse sand and 0.01 cm corresponds to very fine sand.

To be able to store the amounts of data generated from the combined waves and tidal current model over a full tidal cycle, the model was designed to run in intervals of 50 wave periods each. With a wave period of 6 seconds, the model was split into 147 different intervals that results in 44100 seconds, which is equivalent to one tidal period of 12.25 hours.

8.1 Splined data from the model for pure tidal effects

The model for pure tidal flow and the model for only waves was merged together to be able to get combined results for waves and tidal current over a full tidal cycle. The pure tidal results over a full tidal cycle were therefore implemented into the wave model as a one-way implementation.

The horizontal velocity u and vertical velocity v , together with the turbulent kinetic energy k and the dissipation of turbulent kinetic energy ϵ from the model for pure tidal effects was first splined to be able to extract results from all values of time t . The results were splined with a univariate (one variable) interpolation method by Akima (1991) that has the accuracy of a third degree polynomial. Figure 8.1 presents the splined data (dotted lines) plotted against the input data (lines) from the pure tidally driven flow model at 25 cm above the sea-bed. As seen, the splined data follows the input data perfectly throughout the tidal cycle.

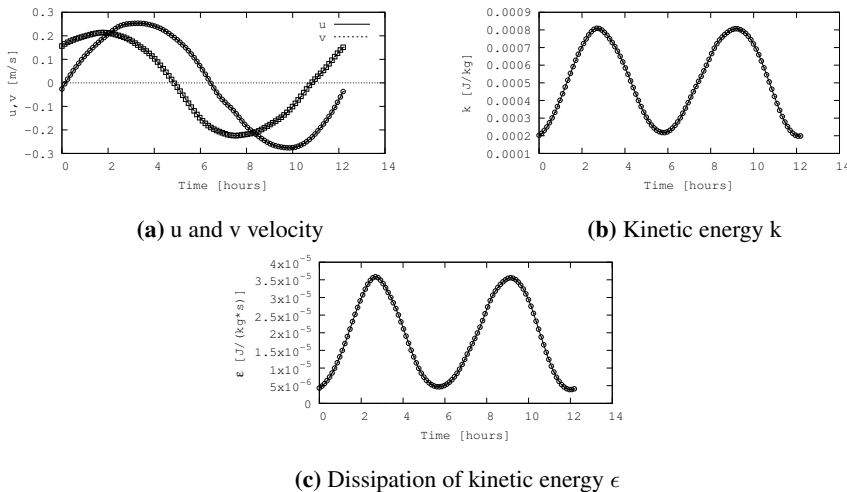
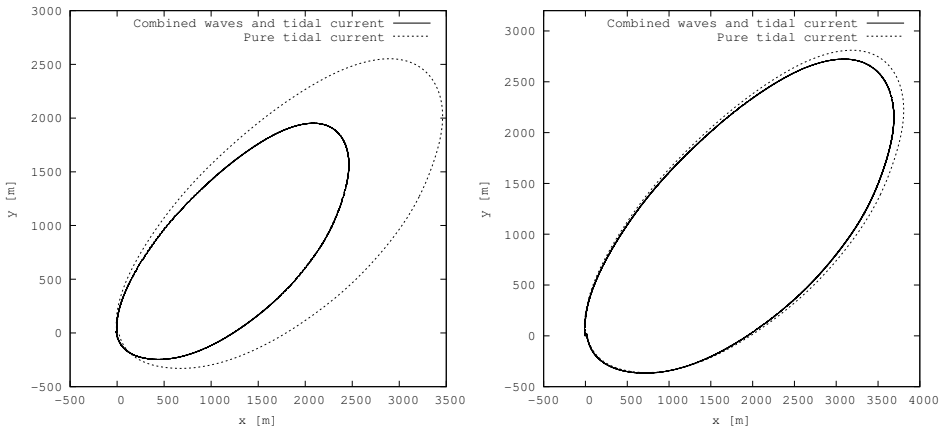


Figure 8.1: Splined results (dotted lines) plotted against the input data (lines) of the horizontal and vertical velocities u and v , the turbulent kinetic energy k and the dissipation of turbulent kinetic energy ϵ

8.2 Particle Trajectories

To see how the combined waves and tidal current develop over large distances, we need to be able to track the particles as they move. Figure 8.2 shows the particle trajectories for combined waves and current flow at 10 and 23 cm above the sea-bed, compared to pure tidal current trajectories (dotted lines). The roughness height z_0 is 0.01 cm. All the ellipses start at the same place at coordinates $(x, y) = (0, 0)$, which means that they are the same around these coordinates. As seen, both the two ellipses for combined waves and tidal current are smaller than their corresponding ellipses for pure tidal current. This is assumed to be caused by increased friction in the flow because of the presence of waves. This introduces the apparent roughness mentioned in chapter 3.4. The consequence of the apparent roughness is that the current above the wave boundary layer on the sea-bed "feels" a larger resistance because of the waves (Grant and Madsen, 1979). This results in reduced velocities and the particles in the combined waves and tidal current flow will hence propagate over reduced distances.

The difference between the combined waves and tidal current ellipse and the pure tidal current ellipse is much larger for 10 cm above the sea-bed, in comparison with 23 cm above the sea-bed. The cause for this is assumed to be that the flow at 10 cm above the sea-bed is closer to the wave-induced boundary layer on the sea-bed, which means that the apparent roughness has a greater influence on the flow closer to the sea-bed.



(a) 10 cm above the sea-bed

(b) 23 cm above the sea-bed

Figure 8.2: Trajectories for 10 and 23 cm above the sea-bed with $z_0 = 0.01$ cm and comparison with pure tidal current ellipses (dotted lines)

Figure 8.3 shows a close-up of the combined waves and tidal current ellipse presented in Figure 8.2a. The close-up has been performed at 6 different locations on the ellipse, starting at the upper left side with a clockwise continuation. As seen, the combined waves and current flow exhibit horizontal oscillations from side to side when the waves and tidal current interact with an angle between each other. As seen from Figure 8.3a, the horizontal velocities imposed by the waves will force the current into a horizontal oscillatory motion. Note that the oscillations does not follow the sinusoidal form, but is rather influenced by the direction of the wave imposed velocities directed in the positive x - direction. From Figure 8.3b, it can be seen that when the angle between the waves and tidal current is zero, in following waves and tidal current, the horizontal oscillations fail to appear. When the waves are normal to the direction of the tidal current, as seen in Figure 8.3c, the oscillations are closer to the sinusoidal form. Figure 8.3d shows a similar pattern as the oscillations in 8.3a, even thou the direction of the tidal current is now towards the wave direction. In Figure 8.3e, where the tidal current direction is directed towards the wave direction, it can be seen a more stretched pattern of the oscillations. At the bottom of the ellipse, where the waves and tidal current is opposing, the oscillations will once again fail to appear, like the case in Figure 8.3b where the waves were following the tidal current direction.

The oscillations in the combined waves and tidal current flow are in conformity with the research performed by A. Davies et al. (1988). Their results showed that the current started veering to form an increased angle between the waves and tidal current after the waves were superimposed on the tidal current. A. Davies et al. (1988) discussed that the reason for this was that different amount of turbulent energy was generated throughout a wave cycle, such that the difference in this turbulent energy causes the combined waves and current direction to change.

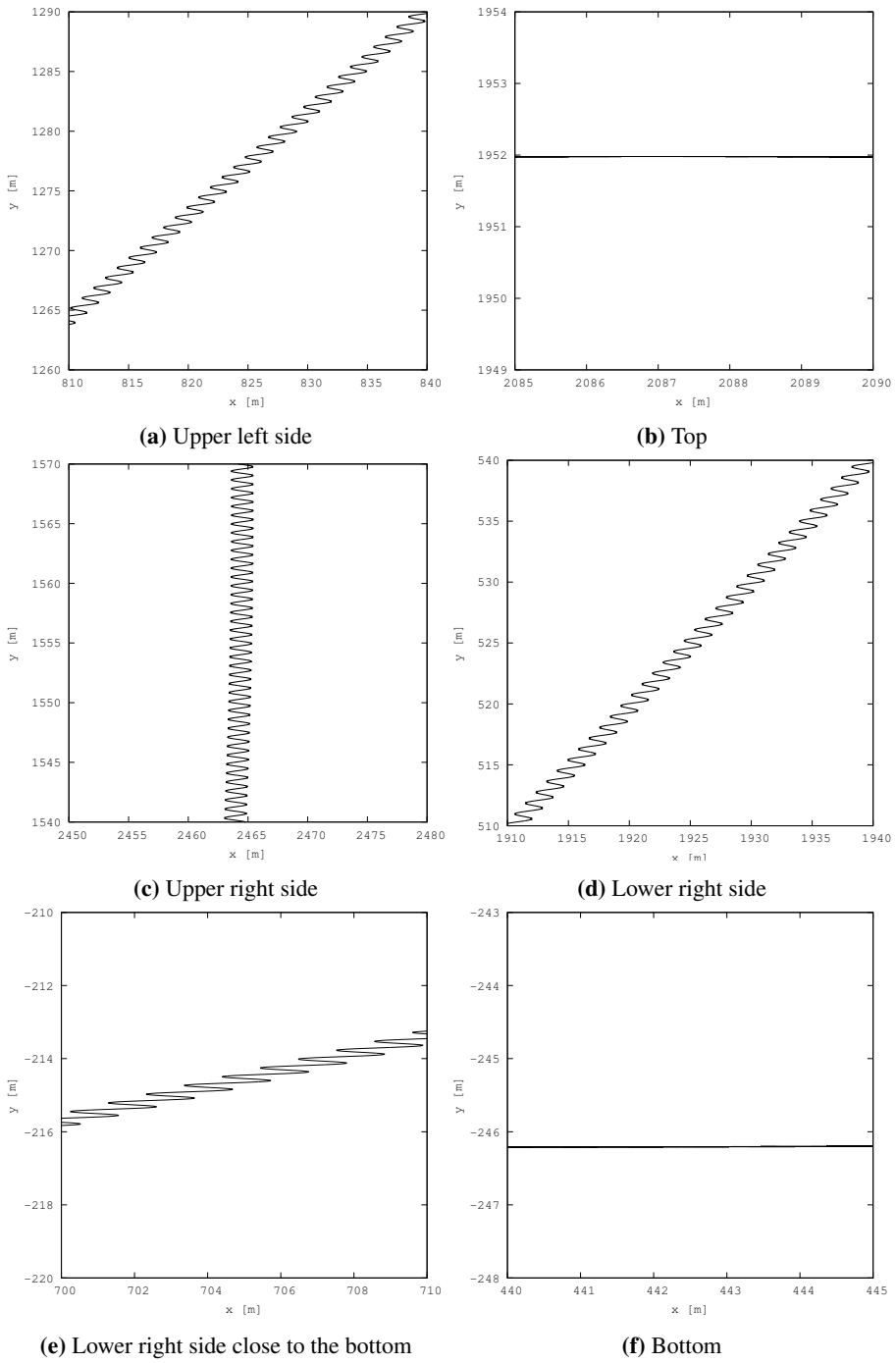


Figure 8.3: Close up of the combined waves and tidal current ellipse at 6 different positions. 10 cm above the sea-bed and with $z_0 = 0.01$ cm

8.3 Effect of Bottom Roughness

Waves impose an extra roughness on the tidal current in a combined waves and tidal current flow. The roughness height z_0 on the sea-bed also plays an important role, as it will increase the friction in the flow. Figure 8.4 shows a representation of the combined waves and tidal current trajectories for the two different values for roughness height, $z_0 = 0.1$ cm and 0.01 cm respectively. Different intervals have been chosen to extract mean velocity profiles, and are marked with numbers in the figure. All simulations in this section have been performed at 10 cm above the seabed.

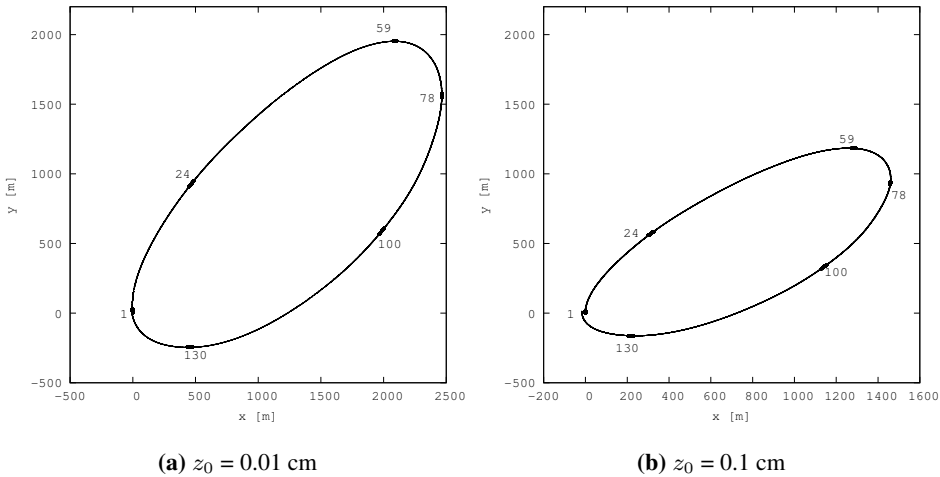


Figure 8.4: The particle trajectory ellipses for combined waves and tidal current 10 cm above the sea-bed with two different values of roughness height. The numbers mark different intervals where mean velocity profiles have been extracted from

Figure 8.5 shows a comparison between the mean velocity profiles in x - direction in different intervals as a function of water column height z for the two different values of roughness height. As seen in Figure 8.5b, the extra roughness on the sea-bed decreases the velocities over the full z domain, but especially close to the sea-bed, where the difference is greater. As seen, the velocity on the top of the ellipse (interval 59) has a smaller magnitude than the velocity on the bottom of the ellipse (Interval 130). This result is unexpected, as it is expected that the velocity at the top of the ellipse, where the waves and tidal current

is following each other, would be of larger magnitude than on the bottom of the ellipse, where the waves oppose the tidal current direction. A potential cause for this, could be that the ellipse is not symmetric.

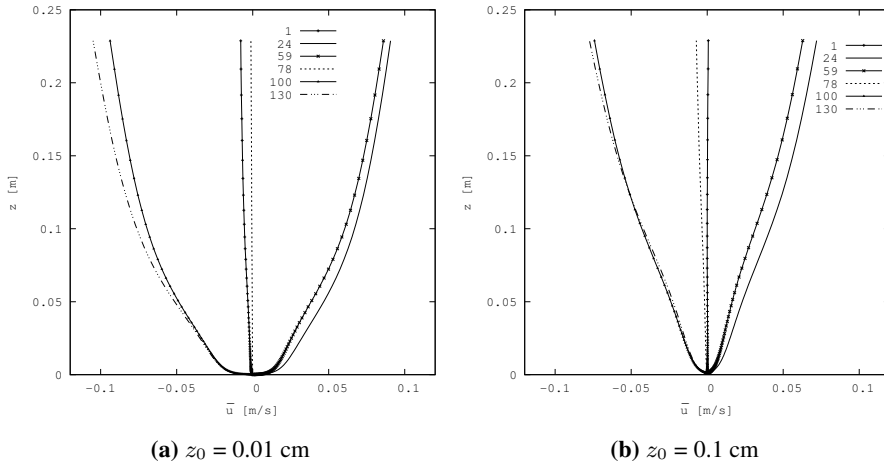


Figure 8.5: Mean velocity profiles for the intervals showed in Figure 8.4

Figure 8.6 shows a comparison between the particle trajectory ellipses that corresponds to the two velocity profiles given in Figure 8.5. Their corresponding ellipses for pure tidal flow have also been included for comparison (dotted lines). As seen, the effect of increased roughness is significant, both for combined waves and tidal current and pure tidal current alone. This states that the extra roughness on the sea-bed has an enormous impact on the particle trajectories because of increased mixing on the sea-bed. The apparent roughness is a function of the relative roughness on the sea-bed, as stated in chapter 3.4. It is therefore reasonable to assume that the reduction in the trajectory ellipses is caused by increased apparent roughness because of increased roughness height z_0 . It is important to note that all simulations have been performed with constant values of roughness height throughout the tidal cycle. Measurements performed by Soulsby et al. (1993), shows that this is a poor estimation. The measurements showed that z_0 varied between 0.1 cm to 1 cm for the maximum and minimum near-bed current respectively. This states that it is utterly important to know the sea-bed environment during field data measurements and numerical simulations, as the roughness height variation can lead to erroneous results.

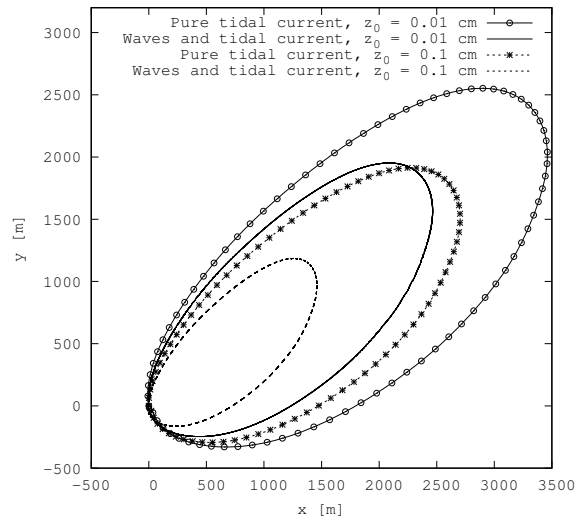


Figure 8.6: Comparison between different values for roughness height z_0 . 10 cm above the sea-bed

Conclusion

The combined effects of waves and pure tidal flow are widely studied and presented in multiple papers and books. However, most of these studies focus on effects through the water column at a given time t . Hence, they do not take into account the horizontal variations in the water column as they develop over time in a tidal cycle. The purpose of present work is to examine the effects from combined sinusoidal waves and tidal current flow over a full tidal cycle, using a one dimensional two-equation turbulence closure model.

The model was first successfully validated for pure tidal flow with field data measurements, and for the wave boundary layer with laboratory experiments. The model was then developed to be able to model the combined effects of waves and tidal current over a full tidal cycle. This is a physical "multiscale" problem that has, to the author's knowledge, never been solved before.

Particle trajectory investigation over a full tidal cycle shows that the combined waves and tidal current exhibit reduced velocities and thus reduced traveling distance compared to pure tidal current alone. The difference between the combined waves and tidal current ellipse and the ellipse for pure tidal current is much larger at 10 cm above the sea-bed in comparison with 23 cm above the sea-bed. The cause for this is assumed to be that the flow at 10 cm above the sea-bed is closer to the wave-induced boundary layer on the sea-bed, which means that the apparent roughness has a greater influence on the flow closer to the sea-bed.

Close-up views of the combined waves and current flow exhibit horizontal oscillations from side to side when the waves and tidal current interact with an angle between each other. This oscillatory pattern changes with the direction of the current, and fail to appear than the angle between waves and tidal current is zero. This is assumed to be caused by change in the generation of turbulent energy over a wave cycle.

The mean velocity profiles for combined waves and tidal current extracted from different intervals in the tidal cycle show that the velocity on the top of the ellipse (following waves and tidal current) has a smaller magnitude than the velocity on the bottom of the ellipse (opposing waves and tidal current). This result is unexpected, as it is expected that the velocity in following waves and tidal current has a larger magnitude than opposing waves and current. A potential cause for this, could be that the ellipse is not symmetric.

The effect of increased bottom roughness z_0 showed to give a significant reduction in the traveling distance of the particles in the trajectory ellipses. It is therefore reasonable to assume that the reduction in the trajectory ellipses is caused by increased apparent roughness because of increased roughness height z_0 , because of the relation between apparent and bottom roughness. This result shows that it is utterly important to know the sea-bed conditions in the area of evaluation.

Chapter 10

Recommendations for further work

The focus in present work has been to develop a functioning numerical model including the combined effects from waves and current. As mentioned, the implementation of waves and current in this thesis has been a one-way implementation. As the waves and current influence each other in a nonlinear way, this will not give an exact representation of the joint current and wave boundary layer. Further work should therefore be focused on getting a more realistic representation of the inter-mutual boundary layer and thus the apparent roughness.

Because of the large time scale of a tidal cycle, where both the waves and current will propagate over large distances, both the vertical and horizontal scale is of importance. Further work should therefore include simulations with nonlinear waves to examine the effects from the mean drift (mass transport) to see what impact these effects have on the tidal current itself.

In present work, zero flux for the turbulent quantities k and ϵ is assumed. This will however give an unrealistic representation as mentioned in Chapter 6.2.2 and will result in inaccurate results further up in the water column. Thus the assumption of zero flux is only valid close to the sea-bed. Further work should therefore include the flux of the turbulent quantities, such that the model would be applicable further up in the water column.

Prediction of sediment transport is of great interest in the prediction of tidal flows, as it is important with regard to forming of river deltas and beaches in coastal areas. As

mentioned in Chapter 3.4, waves will increase the shear stress on the sea-bed. This shear stress will contribute to increased sediment transport. Thus, shear stress analysis of the sea-bed should therefore be included in further work.

No field measurements over a full tidal cycle were found with sufficient quality for present work. Further work should therefore include measurements of tidal flows, as it will add valuable validation data to the combined model.

Bibliography

- Akima, H. (1991). "A method of univariate interpolation that has the accuracy of a third-degree polynomial". eng. In: *ACM Transactions on Mathematical Software (TOMS)* 17.3, pp. 341–366. ISSN: 1557-7295.
- Alfonso, G. (1993). "Reynolds-Averaged Navier-Stokes Equations for Turbulence Modeling". In: *Applied Mechanics Reviews* 62.
- Brown, J. (1989). *Waves, tides and shallow-water processes*. eng. Pergamon Press in association with the Open University.
- Brown, P. N., Byrne, G. D., and Hindmarsh, A. C. (1989). "VODE: A Variable-Coefficient ODE Solver". eng. In: *SIAM Journal on Scientific and Statistical Computing* 10.5, pp. 1038–1051. ISSN: 0196-5204.
- Cengel, Y. A. and Cimbala, J. M. (2014). *Fluid Mechanics: Fundamentals and Applications*. eng. Mc Graw Hill Education.
- Cushman-Roisin Benoit ; Beckers, J.-M. (2011). *Introduction to Geophysical Fluid Dynamics: Physical and Numerical Aspects*. eng. 2nd ed. Vol. 101. International Geophysics. Elsevier Science. ISBN: 0120887592.
- Davies, A., Soulsby, R., and King, H. (1988). "A numerical model of the combined wave and current bottom boundary layer". eng. In: *Journal of Geophysical Research. C. Oceans* 93.C1, pp. 491–508. ISSN: 0148-0227.

BIBLIOGRAPHY

- Dean, R. G. and Dalrymple, R. A. (1991). *Water wave mechanics for engineers and scientists*. eng. Singapore.
- Faltinsen, O. M. (1990). *Sea loads on ships and offshore structures*. eng. Cambridge ocean technology series. Cambridge: Cambridge University Press. ISBN: 0521372852.
- Garrison, T. (2007). *Oceanography : an invitation to marine science*. eng. 6th ed. Belmont, Calif: Thomson/Brooks/Cole. ISBN: 0495112860.
- Grant, W. and Madsen, O. (1979). “Combined wave and current interaction with a rough bottom”. eng. In: *Journal of Geophysical Research* 84, pp. 1797–1808. ISSN: 0148-0227. URL: <http://search.proquest.com/docview/23408288/>.
- Grønningsæter, E. K. (2015). “Tidal Boundary Layer Flow in Coastal Zones”. MA thesis. NTNU.
- Heathershaw, A. and Langhorne, D. (1988). “Observations of near-bed velocity profiles and seabed roughness in tidal currents flowing over sandy gravels”. eng. In: *Estuarine, Coastal and Shelf Science* 26.5, pp. 459–482. ISSN: 0272-7714.
- Holmedal, L. E. (2002). “Wave-Current interactions in the Vicinity of the sea bed. Ph.d”. PhD thesis. Norwegian University of Science and Technology.
- Holmedal, L. E. and Myrhaug, D. (2013). “Combined tidal and wind driven flows and bedload transport over a flat bottom”. eng. In: *Ocean Modelling* 68, pp. 37–56. ISSN: 1463-5003.
- Holmedal, L. E., Myrhaug, D., and Rue, H. (2003). “The sea bed boundary layer under random waves plus current”. eng. In: *Continental Shelf Research* 23.7, pp. 717–750. ISSN: 0278-4343.
- Jensen, B., Sumer, B., and Fredsoe, J. (1989). “TURBULENT OSCILLATORY BOUNDARY-LAYERS AT HIGH REYNOLDS-NUMBERS”. English. In: *Journal Of Fluid Mechanics* 206, pp. 265–297. ISSN: 0022-1120.
- Justesen, P. (1991). “A note on turbulence calculations in the wave boundary layer”. In: *Journal of Hydraulic Research* 29.5, pp. 699–711. URL: <https://doi.org/10.1080/00221689109498985>.
- King H, L. and Davies A, G. (1985). “A Numerical model of the Turbulent Boundary Layer Beneath Surface Waves and tides”. In:

- Myrhaug, D. (2001). *Oceanography: Wind Waves*. eng. Marinteknisk senter, Institutt for marin teknikk.
- (2014). *Oceanography: Currents*. eng. Marinteknisk senter, Institutt for marin teknikk.
- Nielsen, P. (1992). *Coastal bottom boundary layers and sediment transport*. eng. Vol. volume 4. Advanced series on ocean engineering. Singapore: World Scientific. ISBN: 9810204728.
- Pettersen, B. (2004). *Marin Teknikk 3, Hydrodynamikk*. nor. NTNU.
- Pinet, P. R. (2015). *Invitation to oceanography*. eng. Jones & Bartlett Learning.
- Richardson, L. F. (1965). *Weather prediction by numerical process*. Dover books explaining science. New York: Dover Pub.
- Rodi, W. (1993). *Turbulence models and their application in hydraulics : a state-of-the-art review*. eng. 3rd ed. IAHR monograph series. Rotterdam: A.A. Balkema. ISBN: 9054101504.
- Schlichting, H. and Gersten, K. (2017). *Boundary-Layer Theory*. eng. 9th ed. 2017. Berlin, Heidelberg: Springer Berlin Heidelberg. ISBN: 9783662529171.
- Soulsby, R. (1997). *Dynamics of marine sands*. eng. London. ISBN: 0-7277-3955-7.
- Soulsby, R., Hamm, L., Klopman, G., Myrhaug, D., Simons, R., and Thomas, G. (1993). “Wave-current interaction within and outside the bottom boundary layer”. eng. In: *Coastal Engineering* 21.1, pp. 41–69. ISSN: 0378-3839.
- Stokes, G. G. (1846). “1846 Report on recent researches in hydrodynamics”. In:

Appendices

Appendix A

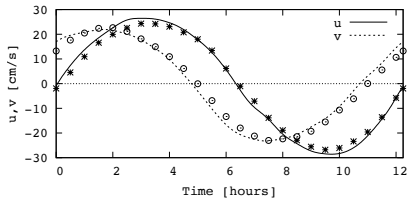
Validation of the pure tidally driven flow model

In the following, the results from the pure tidally driven flow model will be presented. This model was used in the mandatory project thesis in the fall of 2018, leading up to the master thesis. As the project thesis is not published, the most important results are included here. The numerical results for pure tidally driven flow are compared with field data from west of the Isles of Scilly in the Celtic sea measured in 1983 at a water depth of 120 meters presented by King and G. Davies A. (1985). The results are obtained from seven different height levels above the seabed, respectively 1, 2.5, 15, 30, 50, 70, and 90 meters where the free stream velocity is taken from 70 meters above seafloor. Holmedal and Myrhaug (2013) found, after multiple simulations, that an average bottom roughness z_0 of 0.1 cm gave the best fit between the numerical results and field data. According to table 4 in Soulsby (1997), this roughness length corresponds to coarse sand. Since the model is the same as the one used by Holmedal and Myrhaug (2013), the same average roughness of $z_0 = 0.1$ cm was chosen. The Coriolis parameter is $f = 1.112 * 10^{-4}$ and the tidal period is 12.25 hours.

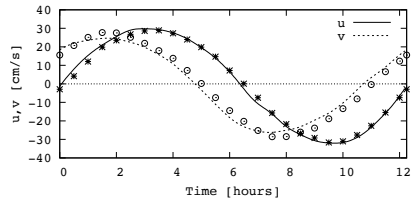
Figure A.1 presents the modeled horizontal and vertical velocity timeseries (lines) compared with field data (points) from King and G. Davies A. (1985) over one tidal period. As

seen, the modeled results fit the field data well, with some deviations. King and G. Davies A. (1985) found from the field measurements used in this work, that there was a nonzero mean between -1.32 cm/s to -2.62 cm/s for the u component and between 0.32 cm/s to 2.71 cm/s for the v component on each elevation. King and G. Davies A. (1985) assumed that this was caused by the wind, and since they only wanted to measure the pure oscillatory tidal flow, these contributions were subtracted from the time series. As mentioned in Chapter 2.1.1, both the moon and sun contribute to the tidal variations. Since the period of rotation of the earth-moon system itself is different from the earth-moon system's rotation around the sun, the elevation in Figure A.1 will not be purely harmonic, and the phase difference between the horizontal velocity components will not be 90° (Holmedal and Myrhaug, 2013).

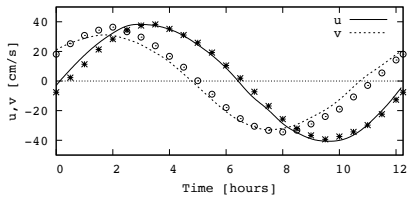
From Figure A.1, it can be seen that the time series close to the sea surface deviates more from the field measurements than for the time series close to the seabed. King and G. Davies A. (1985) argued that the horizontal velocities at 90 meters could possibly be influenced by the surface waves, and therefore chose to use the velocities at 70 m as the free stream velocities U_0 and V_0 . The presence of these surface waves could be a possible explanation of these deviations close to the sea surface.



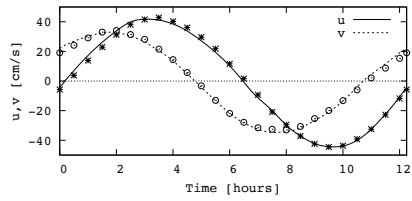
(a) 1 m



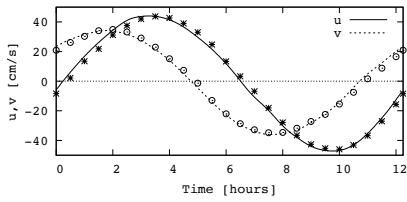
(b) 2.5 m



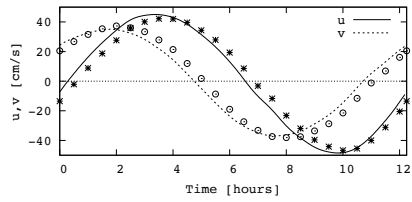
(c) 15 m



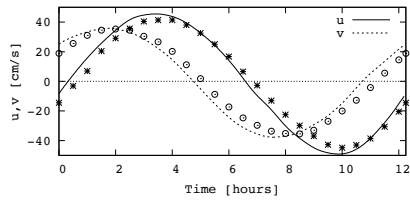
(d) 30 m



(e) 50 m



(f) 70 m



(g) 90 m

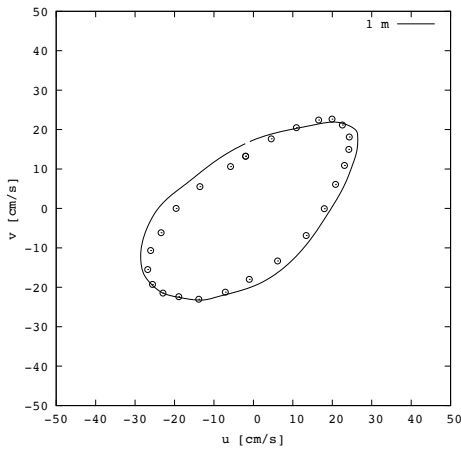
Figure A.1: Velocity time series. Filled lines is u from model, dotted line is v from model, stars are u from field data and circles are v from field data

Figure A.2 shows the tidal ellipses for horizontal velocities presented in Figure A.1. As seen from Figure A.2d and A.2e, the ellipses in the middle of the water column (30 and 50 meters) fits well with the compared field data from King and G. Davies A. (1985). For the ellipses close to the seabed in Figure A.2a and A.2b (1 and 2.5 meters) there is a significant deviation between the model results and the field data. This might be caused by the uncertainty in bottom roughness z_0 . As mentioned, the chosen bottom roughness is constant throughout the tidal cycle and equal to $z_0 = 0.1\text{cm}$. Measurements performed by Soulsby et al. (1993), shows however that choosing a constant roughness length z_0 is a poor estimation. The measurements showed that z_0 varied between 0.1 cm to 1 cm for the maximum and minimum near-bed current respectively. Other experiments performed by Heathershaw and Langhorne (1988) showed an unexpected change in bottom roughness during large movements of marine sediments, and this could also cause deviations in present studies.

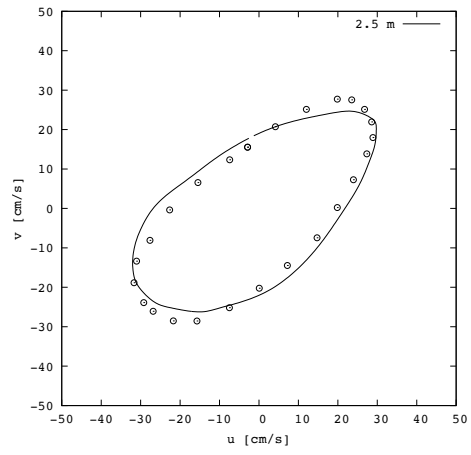
As seen from Figure A.2f and A.2g, the velocity ellipses close to the sea-surface (70 and 90 meters) shows larger deviations from the field measurements compared to the middle of the water column. King and G. Davies A. (1985) expected this to be caused by the presence of surface waves. These surface waves are able to affect the boundary layer at the sea-surface and could therefore affect the tidal velocities close to the sea-surface.

As seen from Figure A.1c, the velocity ellipse for 15 meters above the sea-bed deviates more from the field data than both the ellipses closer to the sea-bed and the ellipses close to the sea-surface. It is hard to point out specific explanation to why this deviation occurs.

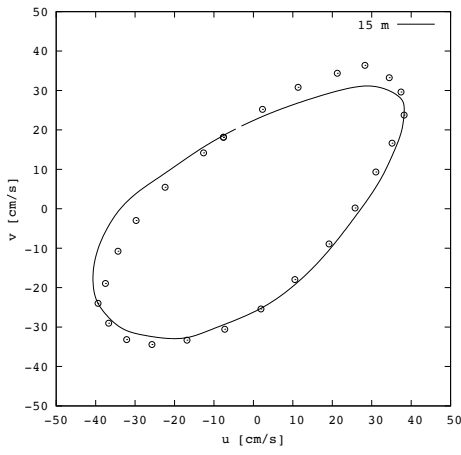
Overall, it can be seen from both Figure A.2 that the numerical model provides results which generally coincide with the field data, and that this rather simple boundary layer model gives a sufficient estimate of the tidal velocities.



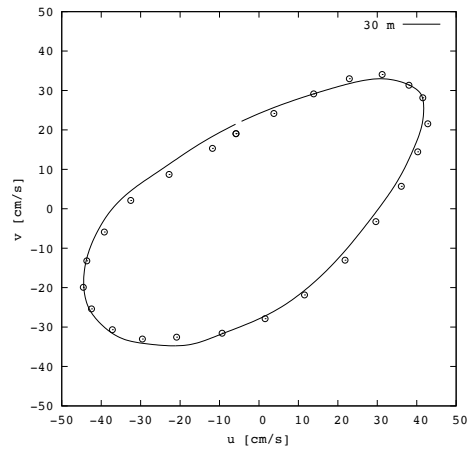
(a) 1 m



(b) 2.5 m

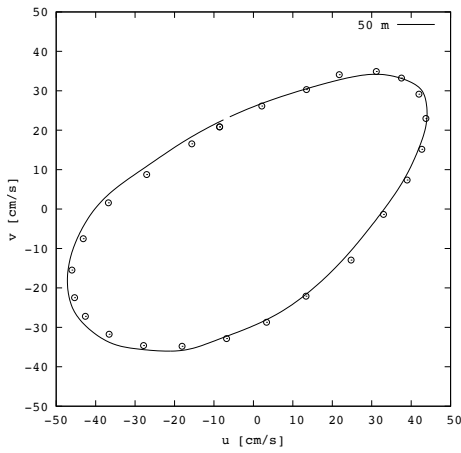


(c) 15 m

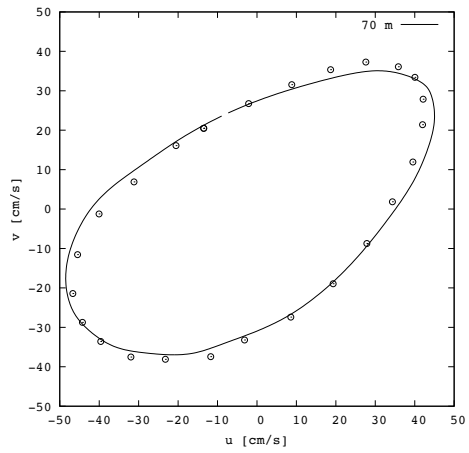


(d) 30 m

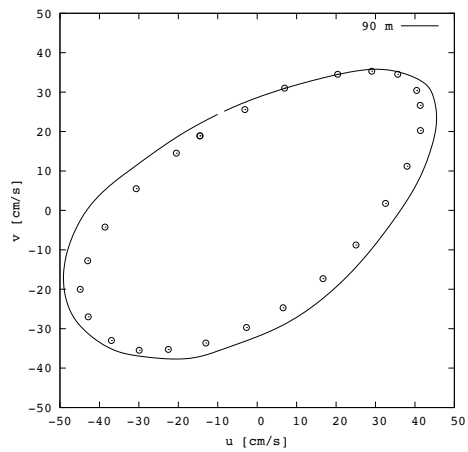
Figure A.2: Tidal velocity ellipses



(e) 50 m



(f) 70 m



(g) 90 m

Figure A.2: Continue

